High-cycle shakedown, ratcheting and liquefaction behavior of anisotropic granular material with fabric evolution: experiments and constitutive modelling

Yi Hong[a], Xuetao Wang[a,*], Lizhong Wang[a,*], Guozheng Kang[b], Zhiwei Gao[c]

[a] *College of Civil Engineering and Architecture, Zhejiang University, Hangzhou, 310056, China*

[b] *Applied Mechanics and Structure Safety Key Laboratory of Sichuan Province, School of Mechanics and Aerospace Engineering, Southwest Jiaotong University, Chengdu, 610031, China*

[c] *James Watt School of Engineering, University of Glasgow, Glasgow, G12 8LT, UK*

Abstract

Although the mechanical response of granular materials strongly depends on the interplay between their anisotropic internal structure (fabric) and loading direction, such coupling is not explicitly considered in existing high-cycle experimental datasets and models. High-cycle experiments on granular specimens specifically prepared with various fabric orientations are presented. It is found that the high-cycle strain accumulation behavior can change remarkably, from shakedown to ratcheting, when the fabric orientation deviates more from the loading direction. Inspired by the experimental observations, a fabric-dependent anisotropic high-cycle model is proposed, by proper recasting of an existing model formulated within Critical State Theory, into the framework of Anisotropic Critical State Theory. The model explicitly accounts for the fabric evolution, which is linked to plastic modulus, dilatancy and kinematic hardening rules. The model can quantitatively reproduce the high-cycle strain accumulation (i.e., shakedown and ratcheting) under drained conditions, as well as pre-liquefaction and post-liquefaction responses granular materials having widely ranged fabric anisotropy, densities and cyclic loading types using a unified set of constants. It exhibits a unique feature of simulating the distinct high-cycle strain accumulation and liquefaction of granular material with various fabric anisotropy, while the existing high-cycle models treat them equally. The successful reproduction of the anisotropic sand element response under high-cycle drained and undrained conditions makes it possible to perform whole life analysis of various foundations on granular soil subjected to high-cycle loading events.

Keywords: Granular material, fabric anisotropy, high-cycle plastic strain accumulation, liquefaction, anisotropic constitutive model

1. Introduction

High-cycle plastic strain accumulation behavior of granular material is a fundamental issue in mechanics and physics, with practical importance in many engineering applications, including offshore wind power, railway and earthquake engineering (Indraratna and Nimbalkar, 2013; Bian et al., 2015; Jardine, 2020; Wang et al., 2021; Page et al., 2021). For example, the marine soil (often made of granular material) supporting offshore wind turbine foundations can experience 10^8 cycles of alternate small-amplitude loading and severe typhoon loading (LeBlanc et al., 2010). Under these long-lasting cyclic loading events, the granular soil can deform towards either shakedown or ratcheting with uncertain evolving trends in stiffness (Houlsby et al., 2017), making it challenging to evaluate the serviceability of the deformation and dynamics-sensitive turbine structure during their whole life operation. Ratcheting or cyclic shakedown of granular materials is not only affected by the stress amplitude but also its state, which is jointly determined by the void ratio (e), effective mean stress (p') and anisotropic microstructure (i.e., fabric). The fabric of granular soil is associated with the orientation of particles, inter-particle contacts, and void spaces (Iwashita and Oda 1999; Sibille et al., 2015; Huang et al., 2020). The effect of fabric anisotropy and its evolution on the high-cycle strain accumulation behavior has been rarely addressed, in the context of experimental study and constitutive modelling.

Experimental investigations into the effect of fabric anisotropy on the monotonic, or low-cycle mechanical behavior of granular soils have been reported by some researchers (Chiaro et al., 2012). These experimental results have shown that the interplay between the fabric anisotropy and the loading direction plays an important role in affecting the mechanical behavior of granular soils, such as dilatancy, stiffness and shear strength. Notably, the granular soil is more dilative with a higher stiffness when the loading direction is more perpendicular to its bedding plane, under otherwise identical conditions. Although these experiments offer valuable insights into the influence of fabric anisotropy, the observed behavior is limited to the granular material response under one or a few loading cycles. Wichtmann (2005) is one of the few to investigate the high-cycle strain accumulation behavior of granular soils up to 10^6 cycles, with primary considerations of different void ratios, stress amplitudes and loading frequencies. The effect of fabric anisotropy on the high-cycle accumulation behavior, however, has not been

specifically intended in Wichtmann (2005)'s study. The dearth of the database on the high-cycle strain accumulation of granular soil with varied fabric anisotropy is a hurdle against the development and validation of fabric-related high-cycle constitutive models.

It remains challenging to predict the cyclic response of granular soil, particularly under high-cycle loading events. A considerable attempt has been made to reproduce the cyclic behavior of granular soil, through either empirical-based (Wichtmann, 2005; Achmus, 2009; Andersen, 2009) or mechanics-based approaches (Dafalias and Manzari, 2004; Corti et al., 2016; Liu et al., 2019; Yang et al., 2022). Although the empirical-based models are highly simplified and can predict the high-cycle mechanical behavior of granular soils at a low computation cost, their predictive capabilities are often limited within the conditions of the tests used for fitting the empirical models (e.g., initial fabric, loading direction and amplitude). Meanwhile, it is very laborious and almost impossible to perform high-cycle tests to experimentally cover all the interplays between the fabric anisotropy and the loading direction. This has necessitated the development of mechanics-based models, with a final goal for a unified description of ratcheting and cyclic shakedown of anisotropic granular soils considering different fabric effects.

Qualitative simulation of high-cycle plastic strain accumulation behavior by mechanics-based models is most widely rendered by incorporating bounding surface plasticity (Dafalias, 1986) along with kinematic hardening (Manzari and Dafalias, 1997; Gajo and Muir Wood, 1999; Li and Dafalias, 2000; Chiu and Ng, 2003; Dafalias and Manzari, 2004; Corti et al., 2016; Petalas et al., 2019; Hong et al, 2021; Wang et al., 2021), micromechanical models (Yin et al., 2010; Song et al, 2023), hypoplastic models (Wu et al., 1996; Liao and Yang, 2021) and crystal plasticity models (Yu et al., 2015). Despite their ability to capture the trends such as accumulation of strain and pore water pressure (for undrained cases), these models tend to simulate a steady ratcheting that significantly over-predicts high-cycle strain accumulation loading cycles, even at a very small cyclic stress amplitude (Niemunis and Herle, 1997; Kang, 2008; Corti, et al., 2016). Such limitation is associated with the model feature that the stiffness in the specific Krieg (1975) type bounding surface plasticity formulation used in these models, as opposed to the Dafalias and Popov (1975, 1976) bounding surface plasticity formulation, hardly changes with loading cycles. This has led to unrealistic prediction of ratcheting response

irrespective of cyclic stress amplitude. This model feature contradicts the experimental and numerical observations, which indicate that the stiffness changes as the internal structure of granular soil cyclically evolves, causing progressive change in strain accumulation rate with loading cycles such as cyclic shakedown (Wichtmann, 2005).

To enable the simulation capability of shakedown under high-cycle loadings, Corti et al. (2016) introduced a memory surface (MS) into a bounding-surface-based model (Gajo and Muir Wood, 1999). The memory surface can be used to capture the effect of cyclic loading history on soil stiffness effectively. This concept was later introduced by Liu et al. (2019) into the SANISAND model (Dafalias and Manzari, 2004). Both models are found by Corti et al. (2016) to reasonably reproduce Wichtmann (2005)'s high-cycle triaxial test results on a granular soil with similar fabric orientations (bedding plane angle β_0=0° with respect to the horizontal direction). Liu et al. (2019)'s model was recently improved by Yang et al. (2022), who detected and addressed the singularity issue in the original formulation of kinematic hardening rule of MS (i.e., possible zeroing of a denominator), with the MS evolution re-formulated to greater simplicity and generality. Though the memory surface in these models is purposely introduced to capture the effect of internal structure evolution during cyclic loading on the stress-train relationship, it does not explicitly incorporate the interplay between fabric anisotropy and loading direction. This limits the models' capability to capture distinct material responses due to changing fabric anisotropy, as observed in monotonic and cyclic experiments (Miura and Toki, 1984; Li and Li, 2009).

Introducing a fabric tensor, as inspired by micromechanical studies, into a constitute model is proven to be effective for simulating the anisotropic behavior of granular soil. For simplicity, most of the earlier studies do not link the fabric anisotropy to the state of the granular soil, or simply define an initial fabric anisotropy which does not evolve with the loading process. The former treatment makes it not possible to describe variable soil states ('loose' or 'dense') at a given set of void ratios and mean effective stress, but with varied fabric anisotropy; While the latter results in a non-uniqueness of the critical state line (Dafalias et al., 2004), which contradicts the micromechanical observations (Li and Li, 2009) and violates the principle of thermodynamics (Li and Dafalias, 2012). These issues have been resolved, with the recently proposed framework of anisotropic critical state theory (ACST) by Li and Dafalias (2012). The

key ideas of ACST are to (a) incorporate a fabric tensor that evolves towards the critical state during shearing, ensuring the uniqueness of the critical state line; (b) introduce the first joint invariant ($A = \mathbf{F}:\mathbf{n}$) between the fabric tensor ($\mathbf{F}$) and the loading direction tensor ($\mathbf{n}$) as the third ingredient (in addition to e and p') featuring soil state, which can be naturally linked with dilatancy and hardening for modelling various fabric-related phenomena. Despite the recent development of some models within the ACST framework, these models were tested only under monotonic and low-cycle (up to a dozen of cycles) for capturing the anisotropic behavior of granular soils. To date, there is still a lack of high-cycle mechanics-based models accounting for fabric anisotropy and evolution, inhibiting reliable whole-life analysis and the design of deformation-sensitive infrastructure (e.g., offshore foundations and railway tracks) on granular geo-materials.

In this work, the above research gaps are addressed by experimentally quantifying the effect of fabric anisotropy on the high-cycle plastic strain accumulation behavior of granular soil, and theoretically developing an anisotropic high-cycle model considering fabric evolution. A novel technique for preparing granular samples with different fabrics was adopted, to support a series of experiments considering various interplays between fabric and loading direction. The experimental results serve as a unique dataset for the development and validation of high-cycle anisotropic models. Based on the experimental observations, an anisotropic model was developed aiming to unify the simulation of high-cycle strain accumulation (shakedown and ratcheting) and liquefaction over a broad range of granular soil states (fabric, void ratio and confining stress) and loading characteristics (including loading path and amplitude) under both drained and undrained conditions using a single set of model constants. It is developed based on Yang et al. (2022)'s sand model within the framework of bounding surface plasticity (Dafalias, 1986) and Critical State Theory (CST). The existing model was extended to incorporate several fabric-related new features into the key model ingredients (plastic modulus, dilatancy and kinematic hardening rules) controlling cyclic behavior, and then cast them into the generalized framework of ACST (Li and Dafalias, 2012). Incorperation of the fabric-related constitutive ingredients suggest the name of SANISAND-FMSf, because it is a member of the SANISAND family of models (Taiebat and Dafalias, 2008). In the name, F represents fabric anisotropy, while M and Sf stand for memory surface and semifluidised state, respectively

(Yang et al., 2022). The proposed high-cycle anisotropic model is validated against the results of experiments on sand with variable states under various loading and drainage conditions.

2. High-cycle experiments for anisotropy granular soil

2.1. Material

Fujian quartz sand, a well-characterized granular material, is employed in this study. The sand with sub-rounded grains has a mean diameter of approximately 0.17 mm and a critical state friction angle of 31° (Yang and Luo, 2015). The maximum and minimum void ratios of the material are 1.027 and 0.627, respectively (Wang et al., 2018).

2.2. Experimental program

The experimental program focuses on the effect of fabric anisotropy, void ratio and cyclic stress amplitude on high-cycle strain accumulation of granular soil. All the experiments were performed under stress-controlled drained cyclic loading using a triaxial apparatus. The experiments were performed on the specimens with different fabric orientations. This is rendered by preparing specimens with three different initial bedding plane angles (β_0=0°, 45°, and 90°) using a new technique, as elaborated in Section 2.3.

Table 1
The experimental program

No.	Mean cyclic deviatoric stress q_{mean} (kPa)	Initial mean effective stress p_0' (kPa)	Cyclic amplitude q_{amp} (kPa)	Initial void ratio e_0	Initial bedding plane angle β_0
1					0°
2	80	200	60	0.67	45°
3					90°
4					0°
5	80	200	60	0.77	45°
6					90°
7					0°
8	80	200	10	0.77	45°
9					90°

For each given β_0, two initial void ratios (e_0=0.67 and 0.77) and two levels of cyclic stress amplitudes q_{amp} (equal to 4% and 24% of the drained shear strength of the specimen with β_0=0°) are considered. In all the tests, an identical initial effective mean stress (p_0'=200 kPa)

was imposed before the application of high-cycle loads. Details of the experimental program are summarized in Table 1.

2.3. Preparing granular specimen with controllable fabric orientation

The conventional approach for granular soil specimens is to deposit dry granular soil vertically through the air into a mechanical loading apparatus, e.g., triaxial apparatus. This approach consistently leads to the specimens with a horizontal bedding plane, in which the long axis of the sand particles is primarily oriented along the horizontal directions (Miura and Toki, 1984).

To prepare the specimens with controllable fabric orientation, a new approach along with a specifically designed apparatus is proposed, as shown in Fig. 1. Following the new approach, dry granular soil was first deposited into a container (length × width × height =500 × 400 × 400 mm) filled with water. An intended void ratio can be achieved by controlling the fall height and the diameter of the nozzle for sand discharge (Borja et al., 2013), which has been readily calibrated. The water-saturated granular soil was then gently cut through by a thin-walled open-tube sampler, which is tightly held by a guide frame fixed at an intended angle (between 0° and 90°) to obtain a desirable fabric orientation. It is worth noting that the inner diameter of the sampler (i.e., 50 mm) is identical to that of a specimen for triaxial testing. The whole package, including the sand container embedded with the sampler, was then gently transferred to a refrigerator for freezing at a temperature of -20 °C. The container and the sampler were designed to be sufficiently rigid to minimize freezing-induced expansion and fabric change. After freezing, the frozen sand was trimmed outside the thin-walled sampler, and then withdrawn from the sampler, to form a specimen of standard dimensions for triaxial testing (diameter=50 mm, height=100 mm).

The specimen with a pre-defined non-horizontal bedding plane was then transferred to the triaxial apparatus and pressurized with a desirable mean effective stress. After complete melting and consolidation of the specimen (i.e., no further water drainage from the bottom of the cell), cyclic loading was imposed according to the experimental program (Table 1).

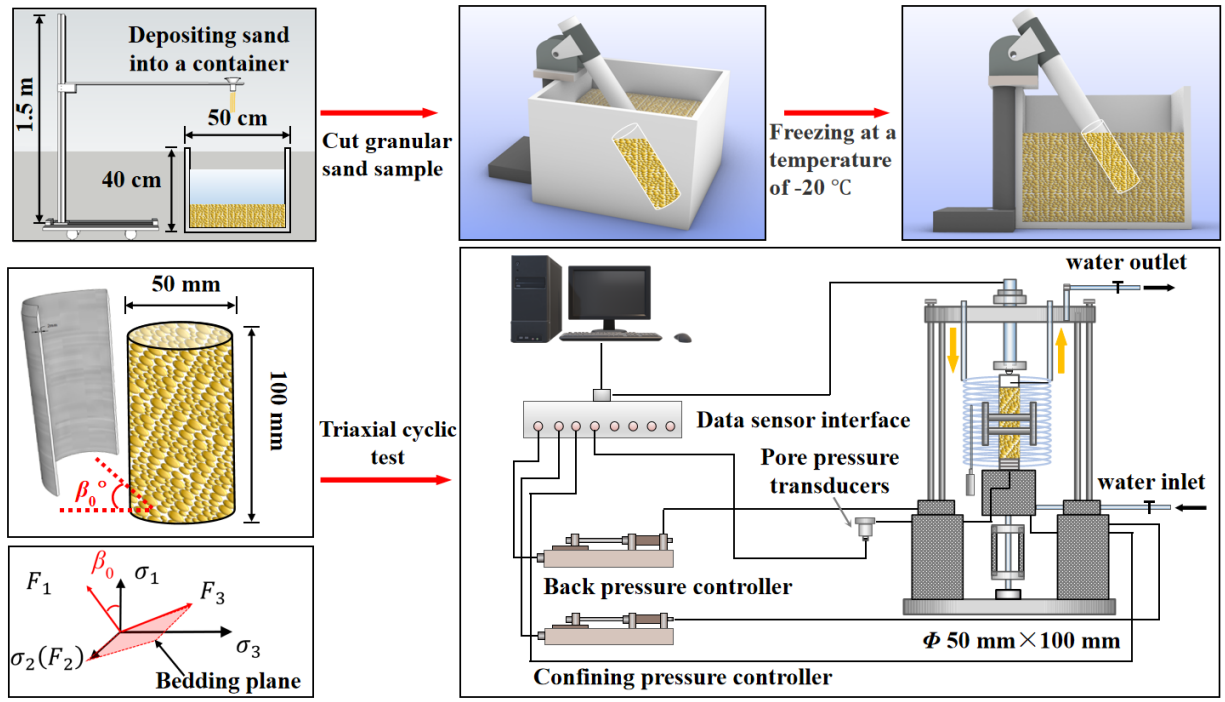

Fig. 1. Schematic diagrams showing the technique for preparing granular specimens with controllable fabric orientation.

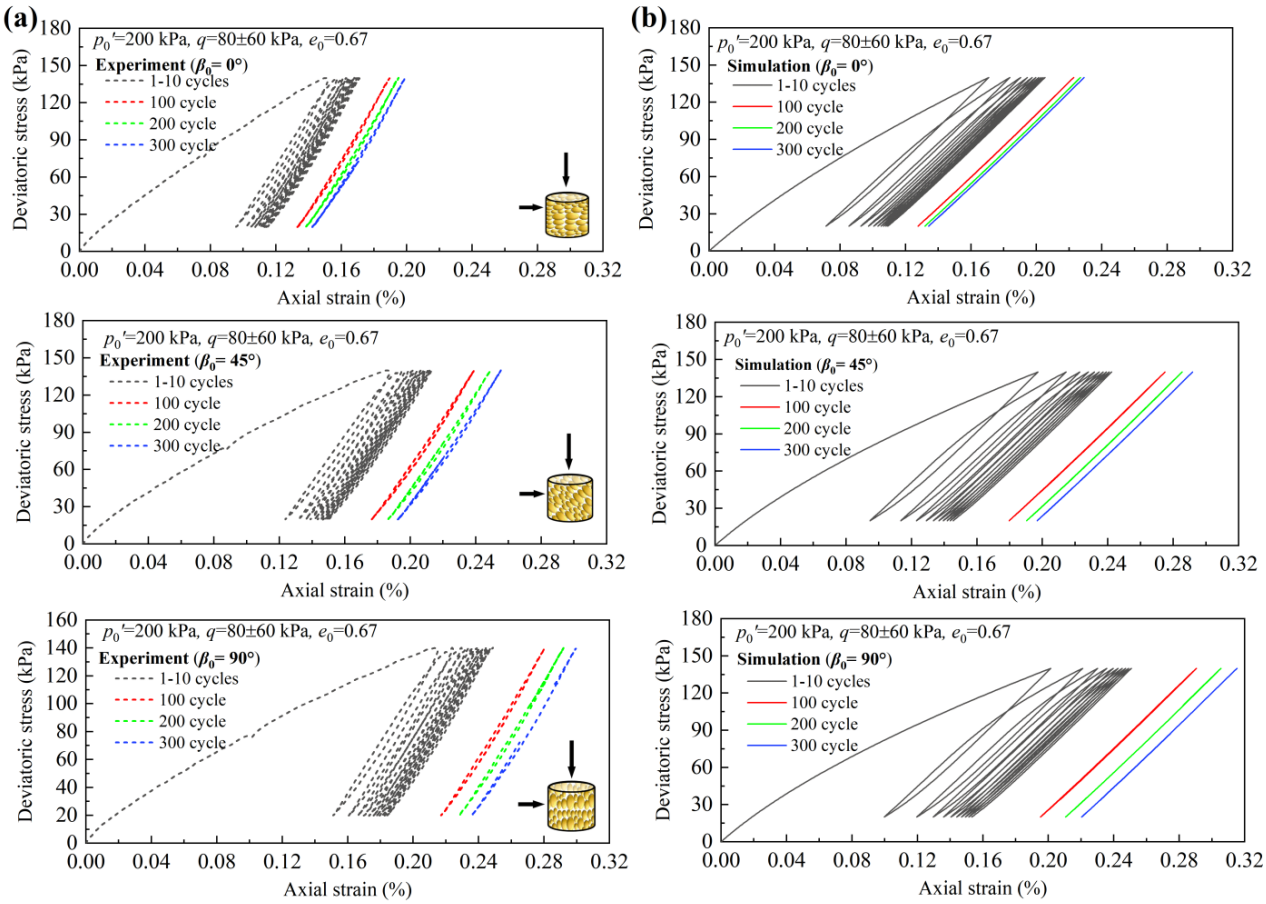

Fig. 2. Effect of β_0 on high-cycle stress strain relationship, with test/simulation settings as p_0'=200 kPa, q=80±60 kPa, e_0=0.67: (a) experimental data for β_0=0°, 45° and 90°. (b) simulation for β_0=0°, 45° and 90°.

2.4. Experimental results and implication for modelling

2.4.1. Influence of fabric orientation, β_0

Figs. 2a shows the measured stress-strain relationships of granular specimens with different fabric orientations (β_0=0°, 45°, 90°) under the same conditions of initial void ratio, mean effective stress and cyclic stress amplitude (e_0=0.67, p_0'=200 kPa, q_{amp}=60 kPa), at selected numbers of cycles (N=1-10, 100, 200 and 300). For each specimen, the high-cycle loading leads to a stiffer response and less plastic dissipation, as indicated by the steeper slope and smaller area during the subsequent stress-strain loops. As β_0 increases, the granular soil becomes less stiff with a broader hysteresis loop and more plastic strain accumulation at any given cycle number.

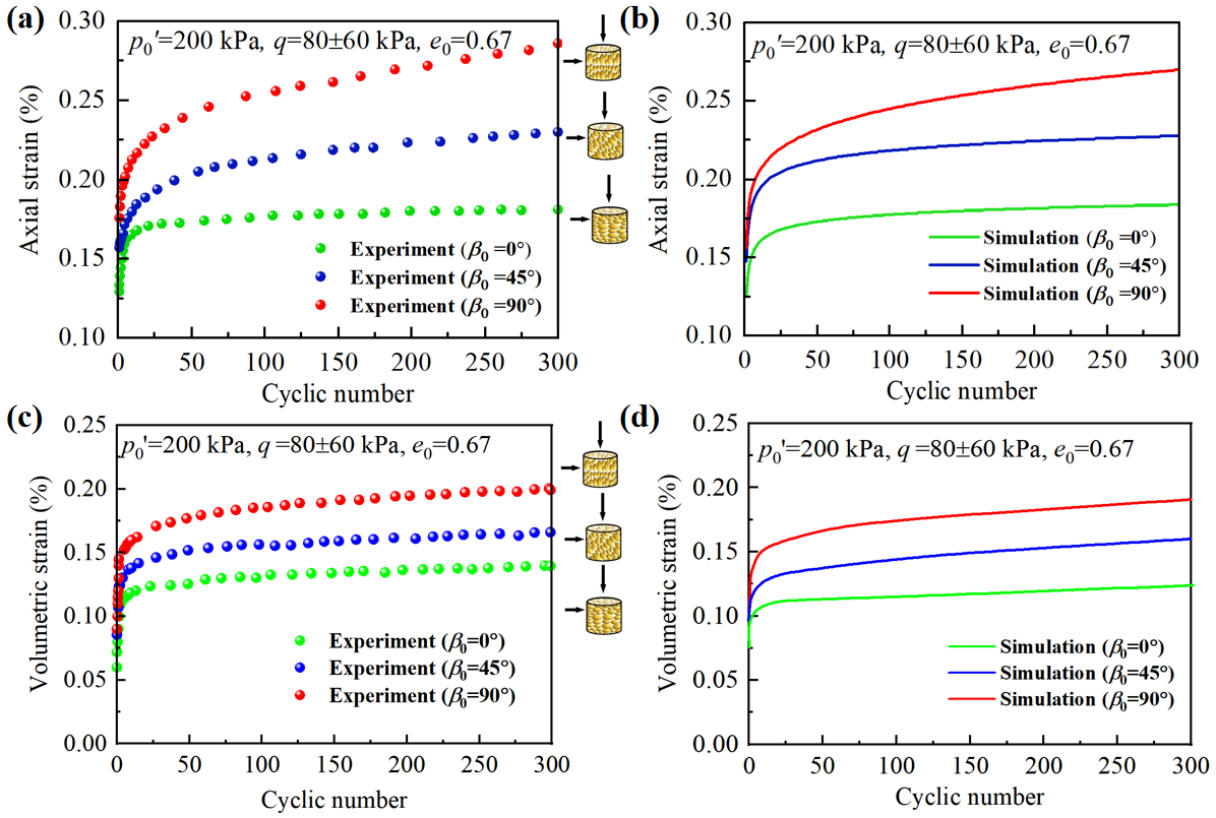

Fig. 3. Influence of β_0 on high-cycle axial and volumetric strain accumulation, with test/simulation settings as p_0'=200 kPa, q=80±60 kPa, e_0=0.67: (a) experimental data for cumulative axial strain; (b) simulation for cumulative axial strain; (c) experimental data for cumulative volumetric strain; (d) simulation for cumulative volumetric strain.

To further reveal the effect of fabric anisotropy on the cyclic shakedown or ratcheting of granular soil, Fig. 3a compares the measured cumulative axial strain with the cycle number for the three specimens (β_0=0°, 45°, 90°). As illustrated, by solely altering the fabric orientation,

the specimens exhibit dramatically different responses to the same stress amplitude, i.e., from shakedown (when β_0=0°) to ratcheting (when β_0=90°). Quantitatively, such a change in fabric orientation causes the cumulative axial strain to increase by 66% (when N=300). The results suggest that fabric does not only affect the strain magnitude, but also critically determines the patterns of axial strain accumulation (i.e., shakedown or ratcheting). Similar trends can also be observed from the accumulation of volumetric strain with the number of cycles (Fig. 3c).

The above experiment observations can be explained from the micro-mechanical perspective that under triaxial compression, a granular soil with a more horizontally aligned bedding plane (smaller β_0) has its orientation of $\mathbf{F}$ aligning closer to the flow direction $\frac{\mathbf{R}^*}{\|\mathbf{R}^*\|}$. This leads to a higher A, which corresponds to a higher density of contact unit normals aligning with the loading direction, and hence larger shearing resistance (Nemat-Nasser, 2000).

2.4.2. Influence of initial void ratio, e_0

Fig. 4a shows the measured axial strain accumulation for relatively loose granular specimens (e_0=0.77), which were tested under otherwise identical conditions as the

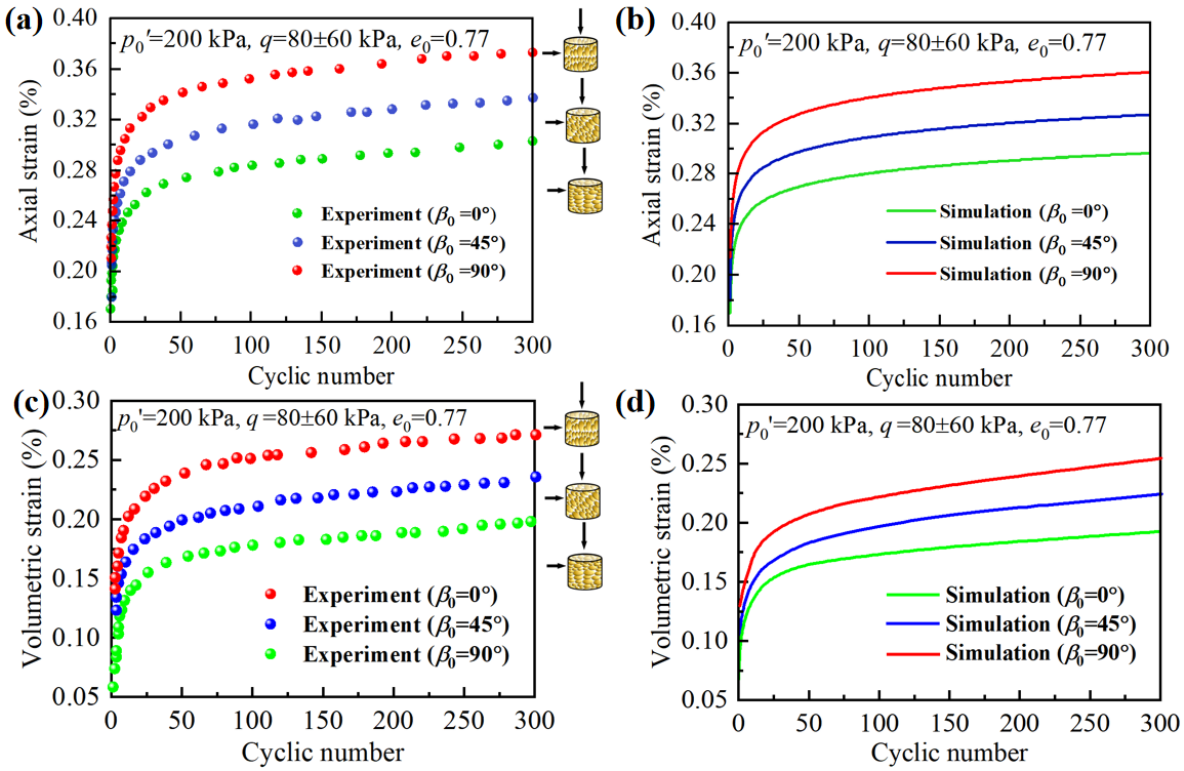

Fig. 4. Influence of β_0 on high-cycle axial and volumetric strain accumulation, with test/simulation settings as p_0'=200 kPa, q=80±60 kPa, e_0=0.77: (a) experimental data for cumulative axial strain; (b) simulation for cumulative axial strain; (c) experimental data for cumulative volumetric strain; (d) simulation for cumulative volumetric strain.

experiments on the relatively dense specimens (e_0=0.67) as presented in Fig. 3a. Comparison between the two figures suggests that for each given β_0, the looser specimen exhibits higher axial strain accumulation, as anticipated. Similar to the relatively dense specimens (e_0=0.67, Fig. 3a), the strain accumulation of the relatively loose specimens (e_0=0.77, Fig. 4a) also depends on the fabric. Increasing β_0 from 0° to 90° facilitates high-cycle strain accumulation, with a percentage increase of 30%. Despite the wide range of fabric orientations (β_0=0°-90°) considered, the relatively loose specimens all exhibit high-cycle ratcheting (Fig. 4a), due to the relatively weak interlocking (and thus lower shear resistance) between the loosely packed particles. The above conclusions also apply to the trends of measured cumulative volumetric strain with the number of cycles, as presented in Fig. 4c.

2.4.3. Influence of cyclic stress amplitude, q_{amp}

The effect of cyclic stress amplitude q_{amp} on the high-cycle axial strain accumulation is also examined, by performing experiments with a lower q_{amp} (i.e., 10 kPa, see Fig. 5a) under otherwise identical conditions as those involving higher q_{amp} (i.e., 60 kPa, see Fig. 4a). Comparison between Fig. 4a and Fig. 5a indicates that for each given β_0, smaller strain accumulation is observed at lower q_{amp}, as anticipated. Despite the relatively loose state of the specimens (e_0=0.77) with different β_0, they all exhibit cyclic shakedown in response to the lower q_{amp} (Fig. 5a). The specimen with a larger β_0 is also found to be less resistant to high-cycle loading A change of β_0 from 0° to 90° leads to an increase of cumulative strain by 80%, and more cycles to achieve shakedown. Similar trends can be observed for the measured accumulation of volumetric strain with cycle number, as presented in Fig. 5c.

2.4.4. Implication for constitutive modelling

In either Fig. 3a, Fig. 4a or Fig. 5a, the granular specimens are purposely prepared with the same combination of e_0 and p_0'. Existing models following the classical isotopic Critical State Theory would treat these specimens as having the same initial state (Been and Jefferies, 1985) and thus exhibiting identical responses to monotonic and cyclic loadings. Such treatment

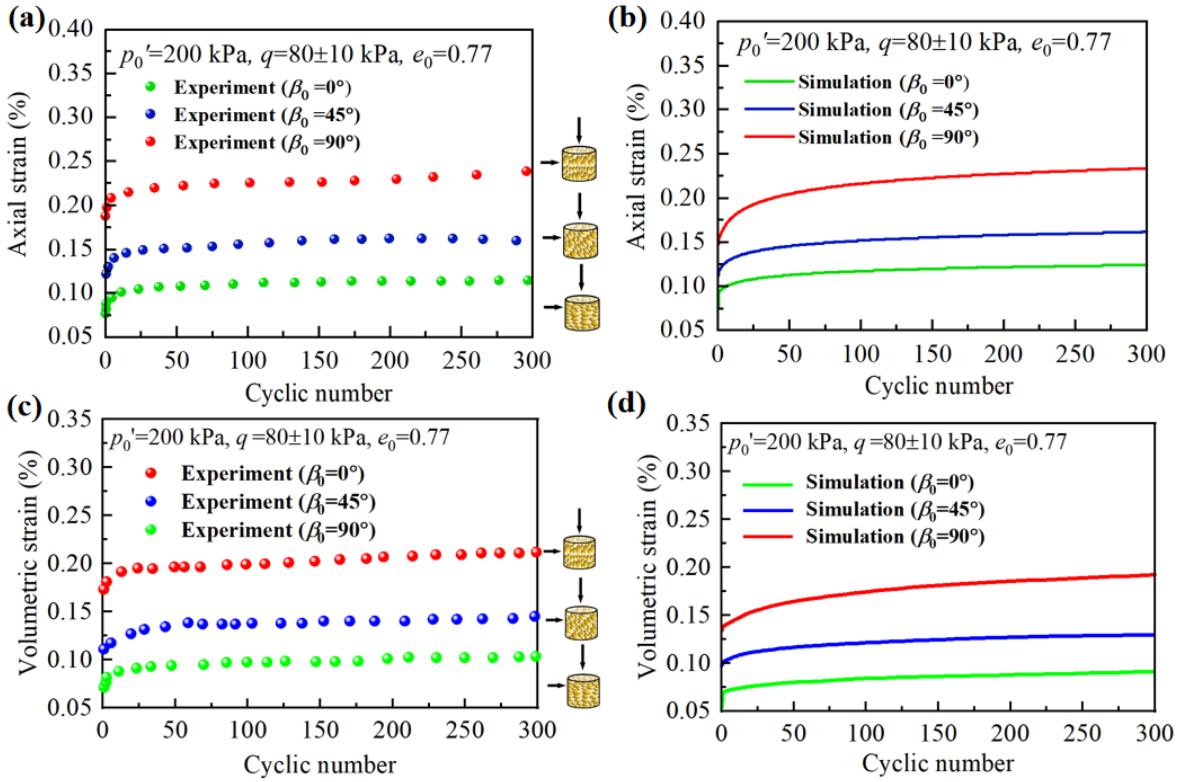

Fig. 5. Influence of β_0 on high-cycle axial and volumetric strain accumulation, with test/simulation settings as p_0'=200 kPa, q=80±10 kPa, e_0=0.77: (a) experimental data for cumulative axial strain; (b) simulation for cumulative axial strain; (c) experimental data for cumulative volumetric strain; (d) simulation for cumulative volumetric strain.

obviously contradicts the experimental observations, i.e., high-cycle strain accumulation for specimens having a given e_0 and p_0' but varied fabric anisotropy could differ by 80% (Fig. 5a). This suggests that the fabric anisotropy and its evolution should be explicitly considered in the description of granular soil state, with direct links to the model ingredients such as hardening, modulus and dilatancy.

3. Model formulation

The proposed anisotropic high-cycle model is built upon two main pillars: a bounding surface sand plasticity model with the memory surface and semifluidised state named SANISAND-MSf model (Yang et al., 2022) and ACST (Li and Dafalias, 2012). The SANISAND-MSf model casting within CST is upgraded by implementing the anisotropic fabric evolution into the soil state, plastic modulus, dilatancy and kinematic hardening rule within the framework of ASCT. Such novel developments have enabled new model capabilities simulating various fabric-dependent monotonic and cyclic responses.

3.1. Notation

The tensor quantities are denoted using bold-face symbols. The symbols $\langle\ \ \rangle$, tr, and : represent the Macauley brackets, trace operator and inner product. $\boldsymbol{\sigma}$ and $\boldsymbol{\varepsilon}$ denote the stress and strain tensor, respectively. $\mathbf{s}$ $(= \boldsymbol{\sigma} - p'\mathbf{I})$ is the deviatoric stress tensor, where p' is the mean effective stress and $\mathbf{I}$ is the second-order identity tensor. The stress ratio tensor that is widely used in the model formulations is $\mathbf{r} = \frac{\mathbf{s}}{p'}$. The deviatoric strain tensor $\mathbf{e}$ is $\mathbf{e} = \boldsymbol{\varepsilon} - \frac{1}{3}\varepsilon_{\mathrm{v}}\mathbf{I}$, where ε_{v} is the volumetric strain defined as $\varepsilon_{\mathrm{v}} = \mathrm{tr}\boldsymbol{\varepsilon}$. The superscripts e and p denote the elastic and plastic strain, respectively.

3.2. A generalized description of state parameters considering fabric anisotropy

Unlikely the conventional isotropic state parameter ψ (Been and Jefferies, 1985; Deng et al.,2021) which ignores fabric effects, an anisotropic state parameter ζ that fully considers the coupling effects of fabric anisotropy A, void ratio e and effective mean stress p' (Li and Dafalias, 2012) is employed in the SANISAND-FMSf model. The difference between ψ and ζ was illustrated and interpreted by Li and Dafalias (2012), as shown in Fig. 6. The isotropic state parameter ψ (Fig. 6a) characterizes the difference between the current void ratio and critical state line (CSL) at the same p', i.e., $\psi = (e, p') = e - e_{\mathrm{c}}(p')$. The critical state line is expressed as

$$e_{\mathrm{c}} = e_{\Gamma} - \lambda_{\mathrm{c}}\left(\frac{p'}{p_{\mathrm{a}}}\right)^{\xi} \tag{1}$$

where e_{c} is the critical state void ratio. λ_{c} and ξ are material constants; p_{a} is the atmospheric pressure (101 kPa). The anisotropic state parameter ζ is featured by the distance between the current void ratio and the dilatancy state line (DSL), which offsets from CSL by a distance of $e_{\mathrm{A}}(A-1)$ depending on fabric anisotropy. ζ is thus expressed as

$$\zeta = \psi - e_{\mathrm{A}}(A-1) \tag{2}$$

where e_{A} is a material constant and A is the anisotropic variable expressed as the joint invariant between the fabric tensor $\mathbf{F}$ and the flow direction tensor $\frac{\mathbf{R}^*}{\|\mathbf{R}^*\|}$

$$A = \mathbf{F}\!:\!\frac{\mathbf{R}^*}{\|\mathbf{R}^*\|} \tag{3}$$

The definition of $\frac{\mathbf{R}^*}{\|\mathbf{R}^*\|}$ and $\mathbf{F}$ are given in Section 3.5 and Section 3.6.1, respectively.

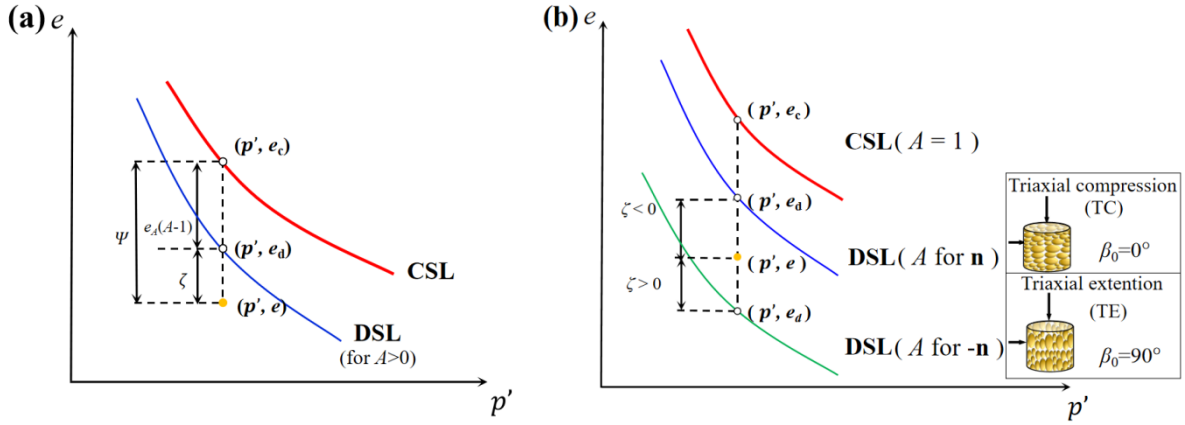

Fig. 6 Definition of DSL, CSL and state parameters in the $e-p'$ space (after Li and Dafalias, 2012).

Eq. (2) is formulated to capture the experimental evidence that, the granular soil state at a given set of e and p' (a given ψ) can be either "loose" (contractive) or "dense" (dilative), depending on the interplay between fabric orientation and flow direction (Yoshimine et al., 1998). This is further elaborated in Fig. 6b, which compares the anisotropic state parameters of two specimens with the same e, p' and stress path (triaxial compression), but different bedding plane angles. For the specimen with a horizontal bedding plane, the major principal strain direction and major fabric orientation are parallel, leading to $A>0$ and thus $\zeta<0$, which features a relatively "dense" state and is more prone to shakedown under cyclic loading. Conversely, the specimen with a vertical bedding plane has $A<0$ and thus $\zeta>0$, featuring a relatively "loose" state that is more susceptible to ratcheting.

3.3. Elastic moduli

The increment of elastic deviatoric strain $\mathrm{d}\mathbf{e}^{\mathrm{e}}$ and volumetric strain $\mathrm{d}\varepsilon_{\mathrm{v}}^{\mathrm{e}}$ of granular soil can be described through the following hypoelastic equation, written as

$$\mathrm{d}\mathbf{e}^{\mathrm{e}}=\frac{\mathrm{d}\mathbf{s}}{2G} \qquad \mathrm{d}\varepsilon_{\mathrm{v}}^{\mathrm{e}}=\frac{\mathrm{d}p\prime}{K} \tag{4}$$

The elastic shear modulus G of the granular soil is calculated using Richard et al. (1970)'s equation, which is pressure- and density-dependent, as follows

$$G=G_0\frac{(2.97-e)^2}{1+e}\sqrt{p'p_{\mathrm{a}}} \tag{5}$$

where G_0 is a material constant and p_{a} (=101kPa) denotes the atmospheric pressure. The elastic bulk modulus K is given below in terms of G and Poisson's ratio ν

$$K=G\frac{2(1+\nu)}{3(1-2\nu)} \tag{6}$$

3.4. Characteristic surfaces for the model

In the SANISAND-FMSf model, the high-cycle strain accumulation and liquefaction of granular soil is described using the bounding surface plasticity enriched with a memory surface. Fig. 7 illustrate the schematic of the model surfaces on the deviatoric stress ratio π-plane. Five surfaces are included, namely yield surface (YS), critical state surface (CS) bounding surface (BS), dilatancy surface (DS) and memory surface (MS). The mapping rules and the image points shown in the figure are explained by Yang et al. (2022), and will be described in the following sub-sections. The formulations of BS, DS and MS are enhanced to describe their dependency on the fabric anisotropy and evolution. The effects of fabric anisotropy on BS and DS were first accounted by Petalas et al. (2019, 2020) and Papadimitriou et al. (2019). While this study incorporates the influence of fabric anisotropy on the evolution of MS, which plays a vital role in capturing the anisotropic high-cycle responses.

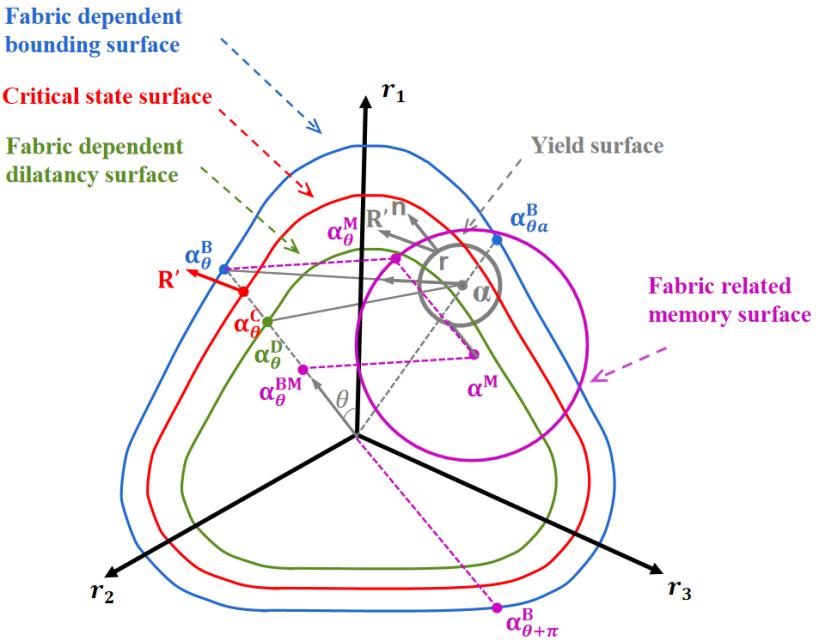

Fig.7. Schematic illustration of the model surfaces and mapping rules on the deviatoric stress ratio π -plane

3.4.1. Yield surface f

The yield surface is an open conical locus enclosing a narrow elastic domain (Dafalias and Manzari, 2004), expressed as

$$f = \sqrt{(\mathbf{s} - p'\boldsymbol{\alpha}) : (\boldsymbol{s} - p'\boldsymbol{\alpha})} - \sqrt{\frac{2}{3}} p' m = 0 \tag{7}$$

The center rotation of the yield surface is governed by the evolution of the back stress-

ratio tensor $\boldsymbol{\alpha}$. The radius of the conical yield surface projected on the π plane is controlled by the model constant m (=0.01). This conical surface in the multi-axial space degenerates into a "wedge" shaped surface in triaxial space, where the bisecting line has a slope α with the wedge opening valued $2mp'$.

3.4.2. Critical state surface f^{CS}

The critical state surface f^{CS} is a conical surface uniquely related to the friction angle of the granular material. The projection of the image back ratio tensor $\boldsymbol{\alpha}$ on the critical state surface is $\boldsymbol{\alpha}_\theta^{\mathrm{CS}}$, as expressed in Eq. (8) (Dafalias and Manzari, 2004; Yang et al., 2022)

$$\boldsymbol{\alpha}_\theta^{\mathrm{CS}} = \sqrt{\frac{2}{3}}[g(\theta)M_{\mathrm{c}} - m]\mathbf{n} \tag{8}$$

where M_{c} is a material constant referred to as the critical stress ratio under triaxial compression; $\mathbf{n}$ is the unit loading direction tensor under the current stress ratio that is perpendicular to the yield surface, expressed as

$$\mathbf{n} = \frac{\mathbf{r}-\boldsymbol{\alpha}}{\sqrt{\frac{2}{3}}m} \tag{9}$$

$g(\theta)$ is an interpolation function describing the shape of the critical state locus that depends on Lode angle θ

$$g(\theta) = \frac{2c}{(1+c)-(1-c)\cos 3\theta} \tag{10}$$

where $c = \frac{M_{\mathrm{e}}}{M_{\mathrm{c}}}$ is a material constant, defining the ratio of the critical stress ratio in triaxial extension M_{e} to triaxial compression M_{c}.

3.4.3. Bounding surface f^{B}

The bounding surface f^{B} is a wide conical surface enabling the model's capability to simulate cyclic loading responses. It sets stress bounds compliant with an evolving state of granular soil. As proposed by Dafalias and Manzari (2004) in SANISAND and later adopted by Yang et al. (2022), The projection of $\boldsymbol{\alpha}$ on the bounding surface is $\boldsymbol{\alpha}_\theta^{\mathrm{B}}$

$$\boldsymbol{\alpha}_\theta^{\mathrm{B}} = \sqrt{\frac{2}{3}}[g(\theta)M^{\mathrm{B}} - m]\mathbf{n} \tag{11}$$

where M^{B} represent the bounding stress ratio. The following expression of M^{B} that accounts for the effect of fabric anisotropy ζ, as originally proposed by Li and Dafalias (2012) and later modified by Theocharis et al. (2017, 2019), is adopted in the model proposed herein

$$M^{\mathrm{B}} = M_{\mathrm{c}}\exp(n^{\mathrm{B}}\langle -\zeta\rangle) \tag{12}$$

where n^{B} is a positive material constant. An important modification was made by Theocharis et al. (2017, 2019) in Eq. (12), compared to that in Li and Dafalias (2012) by using $\langle -\zeta\rangle$ instead of $-\zeta$ to ensure $M^{\mathrm{B}} \geq M$ for sand with any state, based on the observations from DEM experiments (Theocharis et al., 2017, 2019). This treatment is also in line with the original proposition in Manzari and Dafalias (1997) to use $\langle -\psi\rangle$ instead of $-\psi$ for always maintaining $M^{\mathrm{B}} \geq M$. At the critical state (ζ=0), the bounding surface f^{B} coincides with the critical state surface f^{CS}.

3.4.4. Dilatancy surface f^{D}

The dilatancy surface f^{D} differentiates the stress zones associated with the contractive and dilative response as a function of the state of the granular soil. The projection of $\boldsymbol{\alpha}$ on the dilatancy surface is $\boldsymbol{\alpha}_{\theta}^{\mathrm{D}}$, as introduced by the Dafalias and Manzari (2004) and later adopted by Yang et al. (2022)

$$\boldsymbol{\alpha}_{\theta}^{\mathrm{D}} = \sqrt{\frac{2}{3}}[g(\theta)M^{\mathrm{D}} - m]\mathbf{n} \tag{13}$$

where M^{D} represents the dilatancy stress ratio. The expression of M^{D} proposed by Li and Dafalias (2012) as a function of the dilatancy state variable ζ is adopted

$$M^{\mathrm{D}} = M_{\mathrm{c}}\exp(n^{\mathrm{D}}\zeta) \tag{14}$$

where n^{D} is a material constant. At the critical state (ζ=0), the dilatancy surface f^{D} coincides with the critical state surface f^{CS}. Eq. (14) plays a crucial role in the unification of loose and dense sands constitutive description.

3.4.5. Memory surface f^{M}

To enable the simulation of shakedown under high-cycle loading, a memory surface f^{M} is employed for tracking the evolution of internal structure (e.g., fabric anisotropy) during cyclic loading, which affects the plastic hardening and plastic modulus.

The shape of the memory surface is the same as that of the yield surface, which is a conical surface surrounding the stress evolution region. The memory surface is defined by Corti et al. (2016), and later improved by Yang et al. (2022) as expressed below

$$f^{\mathrm{M}} = \sqrt{\left(\boldsymbol{\alpha}_{\theta}^{\mathrm{M}} - \boldsymbol{\alpha}^{\mathrm{M}}\right) : \left(\boldsymbol{\alpha}_{\theta}^{\mathrm{M}} - \boldsymbol{\alpha}^{\mathrm{M}}\right)} - \sqrt{\frac{2}{3}} m^{\mathrm{M}} = 0 \tag{15}$$

where $\boldsymbol{\alpha}^{\mathrm{M}}$ and m^{M} represent the centre and opening size of the memory surface, respectively. $\boldsymbol{\alpha}_{\theta}^{\mathrm{M}}$ is the image point of $\boldsymbol{\alpha}$ on the MS obtained by projection from $\boldsymbol{\alpha}^{\mathrm{M}}$ along $\mathbf{n}$ on it. The hardening law of the memory surface is enhanced in the model, by explicitly incorporating the fabric anisotropy and evolution into the formulations governing the translation and size change of the memory surface (i.e., $\mathrm{d}\boldsymbol{\alpha}^{\mathrm{M}}$ and $\mathrm{d}m^{\mathrm{M}}$, respectively), as detailed in Section 3.6.2.

3.4.6. Plastic hardening and plastic modulus

According to the bounding surface plasticity theory (Dafalias 1986), the kinematic hardening law of back-stress ratio $\boldsymbol{\alpha}$ and the plastic modulus K_{p} both depend on the distance between $\boldsymbol{\alpha}_{\theta}^{\mathrm{B}}$ and $\boldsymbol{\alpha}$, as expressed in Eq. (16) and Eq. (17) (Dafalias and Manzari , 2004; Yang et al., 2022)

$$\mathrm{d}\boldsymbol{\alpha} = \frac{2}{3}\langle L \rangle h\left(\boldsymbol{\alpha}_{\theta}^{\mathrm{B}} - \boldsymbol{\alpha}\right) \tag{16}$$

$$K_{\mathrm{p}} = \frac{2}{3} p' h\left(\boldsymbol{\alpha}_{\theta}^{\mathrm{B}} - \boldsymbol{\alpha}\right) : \mathbf{n} \tag{17}$$

where h is a hardening coefficient of the BS formulation, as described later in Eq. (28). It is worth noting that the plastic modulus K_{p} as formulated in Eq. (17) is not independently proposed from Eq. (16), but is obtained based on imposing the condition of consistency on Eq. (7) of the yield surface, as proposed by Dafalias (1986).

3.5. Plastic flow rule

Non-associated plastic flow rule is adopted, as revealed from discrete element analysis for granular materials (Li and Dafalias, 2015; Karapiperis et al., 2020). The increments of plastic deviatoric strain $\mathrm{d}\mathbf{e}^{\mathrm{p}}$ and plastic volumetric strain $\mathrm{d}\varepsilon_{\mathrm{v}}^{\mathrm{p}}$ can be expressed by Eq. (18) and Eq. (19), respectively

$$\mathrm{d}\mathbf{e}^{\mathrm{p}} = \langle L \rangle \mathbf{R}^{*} \tag{18}$$

$$\mathrm{d}\varepsilon_{\mathrm{v}}^{\mathrm{p}} = \langle L \rangle D \tag{19}$$

where L is the plastic multiplier or loading index, the latter name adopted because the sign of L defines loading when $L>0$, neutral loading when $L=0$ and unloading when $L<0$, hence the use of Macauley brackets in Eq. (18) and Eq. (19). $\mathbf{R}^{*}$ and D are the tensor of deviatoric

plastic flow direction and coefficient of dilatancy, respectively. Formulations of D considering the fabric anisotropy are presented in Section 3.6.2.

$\mathbf{R}^*$ is formulated as proposed by Yang et al. (2022), which unifies the description of plastic flow direction under both proportional and non-proportional cyclic loading

$$\mathbf{R}^* = \left(\frac{\left\langle \left\| \boldsymbol{\alpha}^{\mathrm{B}}_{\theta_\alpha} \right\| - \|\boldsymbol{\alpha}\| \right\rangle}{\left\| \boldsymbol{\alpha}^{\mathrm{B}}_{\theta_\alpha} \right\|}\right)^2 \mathbf{n} + \left[1 - \left(\frac{\left\langle \left\| \boldsymbol{\alpha}^{\mathrm{B}}_{\theta_\alpha} \right\| - \|\boldsymbol{\alpha}\| \right\rangle}{\left\| \boldsymbol{\alpha}^{\mathrm{B}}_{\theta_\alpha} \right\|}\right)^2\right] \frac{\mathbf{R}'}{\|\mathbf{R}'\|} \tag{20}$$

Eq. (20) describes the direction of the deviatoric strain tensor $\mathbf{R}^*$ as an interpolation between the loading direction tensor $\mathbf{n}$ and the unit norm $\frac{\mathbf{R}'}{\|\mathbf{R}'\|}$ which is the direction of the deviatoric strain tensor commonly adopted in the SANISAND family. The form of $\mathbf{R}'$ was proposed by Dafalias and Manzari (2004) as $\mathbf{R}' = B\mathbf{n} - C\left(\mathbf{n}^2 - \frac{1}{3}\mathbf{I}\right)$, where B and C are functions of the Lode angle, i.e., $B = 1 + \frac{3(1-c)}{2c} g(\theta) \cos 3\theta$ and $C = 3\sqrt{\frac{3}{2}}\frac{1-c}{c} g(\theta)$. The interpolation function $\frac{\left\langle \left\| \boldsymbol{\alpha}^{\mathrm{B}}_{\theta_\alpha} \right\| - \|\boldsymbol{\alpha}\| \right\rangle}{\left\| \boldsymbol{\alpha}^{\mathrm{B}}_{\theta_\alpha} \right\|}$ characterizes the relative distance between the back-stress ratio $\boldsymbol{\alpha}$ and its projection on the bounding surface $\boldsymbol{\alpha}^{\mathrm{B}}_{\theta_\alpha}$ (Yang et al., 2022).

3.6. Incorporation of fabric evolution into dilatancy and hardening rules of memory surface

3.6.1. Fabric tensor and its evolution

The fabric tensor is used generically as a symmetric traceless tensor that is related to the internal structure of sand. For an initially cross-anisotropic soil, the initial fabric tensor can be expressed as below when the x-y plane is the deposition plane, written as

$$\mathbf{F} = \begin{pmatrix} F_{zz} & & \\ & F_{xx} & \\ & & F_{yy} \end{pmatrix} = \sqrt{\frac{2}{3}} \begin{pmatrix} F_0 & & \\ & -\frac{F_0}{2} & \\ & & -\frac{F_0}{2} \end{pmatrix} \tag{21}$$

where F_0 is the initial degree of fabric anisotropy. If the deposition direction does not align with the z-axis, the corresponding orthogonal transformation is needed to obtain the initial fabric tensor $\mathbf{F}$.

Following Petalas et al. (2019; 2020) and Papadimitriou et al. (2019) who first introduced fabric anisotropy into SANISAND, the model proposed in this study also assumes the fabric to evolve towards the flow direction

$$\mathrm{d}\mathbf{F} = \langle L \rangle k_{\mathrm{f}} \left(\frac{\mathbf{R}^*}{\| \mathbf{R}^* \|} - \mathbf{F} \right) e^{A} \tag{22}$$

where $\mathrm{d}\mathbf{F}$ is the rate of fabric evolution; k_{f} is a model constant controlling the rate of fabric evolution. This simplified form only needs one parameter to determine the evolution of the fabric tensor. An additional term e^{A} is introduced to describe the rate of fabric evolution observed in micromechanical studies: under the same plastic strain rate, the material under triaxial compression exhibits a faster rate of fabric evolution than the specimen under triaxial tension. Note that A is higher in triaxial compression than triaxial extension when the soil fabric (direction and magnitude) is the same. This finding is in line with the simulation results by Discrete Element Method (Yimsiri and Soga, 2015).

3.6.2. Fabric-related dilatancy

The dilatancy function is proposed based on Dafalias and Manzari (2004) and Yang et al. (2022)'s formulation, which is extended to consider fabric effects by adding a new term $\exp[k_1(1-A)]$ and replacing the state parameter ψ with ζ, as follows:

$$D = \left\{ A_0 g(\theta)^{-n_{\mathrm{g}}} (1 + \langle \mathbf{z} : \mathbf{n} \rangle)(\boldsymbol{\alpha}_\theta^{\mathrm{D}} - \boldsymbol{\alpha}) : \mathbf{n} \right\} \underbrace{\exp[k_1(1-A)]}_{\textbf{fabric dependent}} \tag{23}$$

where n_{g} and k_1 are two material constants. A_0 is the dilatancy parameter which remains constant in the pre-liquefication stage, but degrades in the post-liquefaction stage, as formulated and explained later in Eq. (35) of Section 3.7. $g(\theta)^{-n_{\mathrm{g}}}$ is introduced to control the shifting of the stress-strain loops towards extension (Yang et al., 2022). $\mathbf{z}$ is the fabric-dilatancy tensor variable introduced by Dafalias and Manzari (2004) to realistically simulate cyclic mobility and liquefaction. The evolution of $\mathbf{z}$ and its consequence on the improvement of simulation capability is explained in detail by Dafalias and Manzari (2004).

The new fabric-dependent term $\exp[k_1(1-A)]$ is introduced in light of observations from many experiments on specimens with different β_0 (e.g., Oda et al., 2001). Some of the test results in Oda et al. (2001) are shown in Fig. 23 in the model validation section. The proposed dilantacy function (Eq. (23)) phenomenologically describes the following key features of fabric dependent dilatancy:

1. For β_0 =0° (e.g., specimens prepared in a usual way), A is larger in TC than TE, which makes D smaller in TC. The model thus predicts a more dilative response and smaller cyclic strain accumulation on the TC side.

2. For β_0 =90°, A in TC is smaller than TE, with a larger D in TC, and thus rendering a less dilative response and larger cyclic strain accumulation on the TC side.

3.6.3. Fabric-related hardening rules of memory surface

The evolution of the memory surface $\boldsymbol{\alpha}_\theta^{\mathrm{M}}$ is primarily controlled by the change in the opening size of the memory surface m^{M} and the translation of the central position $\boldsymbol{\alpha}^{\mathrm{M}}$ during cyclic loading, expressed as

$$\boldsymbol{\alpha}_\theta^{\mathrm{M}} = \boldsymbol{\alpha}^{\mathrm{M}} + \sqrt{\frac{2}{3}} m^{\mathrm{M}} \mathbf{n} \tag{24}$$

In the existing high-cycle models (Yang et al., 2022), fabric-related variables are not explicitly formulated in the hardening rules. A fabric-related anisotropic hardening rule is therefore proposed based on Yang et al. (2022)'s formulation, where the effect of A is incorporated into its first term for describing the fabric-dependent expansion rate of MS

$$\begin{aligned} \mathrm{d}m^{\mathrm{M}} = \langle L \rangle \left\{ \sqrt{\frac{2}{3}} c_c h^{\mathrm{M}} \langle (\boldsymbol{\alpha}_\theta^{\mathrm{B}} - \boldsymbol{\alpha}_\theta^{\mathrm{M}}) : \mathbf{n} \rangle \underbrace{\exp[-k_2(1-A)]}_{\textbf{fabric dependent}} \right\} \\ - \langle L \rangle \left\{ -\frac{m^{\mathrm{M}}}{\varsigma} \left| (\boldsymbol{\alpha}_\theta^{\mathrm{B}} - \boldsymbol{\alpha}_\theta^{\mathrm{M}}) : \mathbf{n} \right| \langle -D \rangle \right\} \end{aligned} \tag{25}$$

In the above equation, the first and the second terms feature expansion and contraction of MS, respectively. c_c=1 is usually a default value, proposed in Corti et al. (2016). ς and k_2 are two material constants which, respectively, control the expansion and contraction rates of the memory surface. The first term is enhanced with the new addition of a fabric dependent ingredient $\exp[-k_2(1-A)]$, as proposed in the light of the experimental observations made in this study (see Section 2). It is particularly useful for predicting the fabric-dependent high-cycle drained response, which is a primary feature of the SANISAND-FMSf model. Notably, Eq. (25) predicts a faster expansion of memory surface for repeatedly loaded specimens with higher A, which renders longer bounding-to-memory surface distance $(\boldsymbol{\alpha}_\theta^{\mathrm{B}} - \boldsymbol{\alpha}_\theta^{\mathrm{M}}) : \mathbf{n}$ and thus larger plastic modulus K_{p} (to be derived in Eq. (31)), with a consequence of a higher potential to the shakedown.

It is worth noting that the two terms in Eq. (25) are specifically treated following Yang et al. (2022)'s way, to avoid two traps which may appear in the isotropic hardening rule of MS in

the platform model (Yang et al., 2022):

1. A Macaulay bracket is applied to the first term (i.e., $\langle(\boldsymbol{\alpha}_\theta^{\mathrm{B}}-\boldsymbol{\alpha}_\theta^{\mathrm{M}}):\mathbf{n}\rangle$) to avoid the occurrence of negative m^{M}.
2. The quantity of $\left|(\boldsymbol{\alpha}_\theta^{\mathrm{B}}-\boldsymbol{\alpha}_\theta^{\mathrm{M}}):\mathbf{n}\right|$ is introduced to the second term for addressing the singularity issue caused by $(\boldsymbol{\alpha}_\theta^{\mathrm{B}}-\boldsymbol{\alpha}_\theta^{\mathrm{M}}):\mathbf{n}$=0, which will appear in the denominator of the MS kinematic hardening rule $\mathrm{d}\boldsymbol{\alpha}^{\mathrm{M}}$, as derived in Eq. (26).

It is commonly assumed that the memory surface coincides with the yield surface at the original loading point ($\boldsymbol{\sigma}\equiv\boldsymbol{\sigma}^{\mathrm{M}}, L=L^{\mathrm{M}}$) (Corti et al., 2016; Yang et al., 2022). With this assumption, the fabric-dependent kinematic hardening rule of the memory surface $\mathrm{d}\boldsymbol{\alpha}^{\mathrm{M}}$ can be derived from Eq. (25) and the condition of consistency of the memory surface ($\frac{\partial f^{\mathrm{M}}}{\partial\boldsymbol{\sigma}^{\mathrm{M}}}:\mathrm{d}\boldsymbol{\sigma}^{\mathrm{M}}=-\left(\frac{\partial f^{\mathrm{M}}}{\partial\boldsymbol{\alpha}^{\mathrm{M}}}:\mathrm{d}\boldsymbol{\alpha}^{\mathrm{M}}+\frac{\partial f^{\mathrm{M}}}{\partial m^{\mathrm{M}}}\mathrm{d}m^{\mathrm{M}}\right)=L^{\mathrm{M}}K_p^{\mathrm{M}}$), as

$$\mathrm{d}\boldsymbol{\alpha}^{\mathrm{M}}=\frac{2}{3}\langle L\rangle h^{\mathrm{M}}\left(\boldsymbol{\alpha}_\theta^{\mathrm{B}}-\boldsymbol{\alpha}_\theta^{\mathrm{M}}\right) \tag{26}$$

$$h^{\mathrm{M}}=\frac{1}{1+c_c\mathcal{H}\left[\left(\left(\boldsymbol{\alpha}_\theta^{\mathrm{B}}-\boldsymbol{\alpha}_\theta^{\mathrm{M}}\right)\right):\mathbf{n}\right]\underbrace{\exp[-k_2(1-A)]}_{\textbf{fabric dependent}}\left\{h+\sqrt{\frac{3}{2}}\frac{m^M\mathrm{sgn}\left[\left(\left(\boldsymbol{\alpha}_\theta^{\mathrm{B}}-\boldsymbol{\alpha}_\theta^{\mathrm{M}}\right)\right):\mathbf{n}\right]\langle -D\rangle}{\varsigma}\right\}} \tag{27}$$

In Eq. (27), the Heaviside function renders $\mathcal{H}[x]=1$ for $x\geq 0$, and $\mathcal{H}[x]=0$ for $x<0$. The sign function works as that $\mathrm{sgn}[x]=1$ for $x>0$, $\mathrm{sgn}[x]=0$ for x =0, and $\mathrm{sgn}[x]=-1$ for x <0. The appearance of both $\mathcal{H}$ and sgn functions, is due to the use of < > and | | in the first and second terms, respectively, of Eq. (25). Such treatments following Yang et al. (2022) lead to avoidance of the singularity issue arising from zeroing in the denominator of h^{M}, which may possibly occur in the platform model (Yang et al., 2022).

3.6.4. Fabric-dependent plastic modulus

The effect of fabric anisotropy on the high-cycle plastic strain accumulation is primarily described by incorporating the memory-to-yield distance $(\boldsymbol{\alpha}^{\mathrm{M}}-\boldsymbol{\alpha}):\mathbf{n}$ into the plastic modulus K_{p} through the hardening coefficient h (Eq. (17)). The linear dependence of h on A was first introduced by Li and Dafalias (2012), while a nonlinear dependence (h as a function

of $e^{k_3 A}$) was introduced by Papadimitriou et al. (2019) and Petalas et al. (2020). Following the latter two, the coefficient h in the new SANISAND-FMSf model is also incorporated with fabric effect by introducing the term $e^{k_3 A}$ into h which was originally formulated in the basic model SANISAND-MSf (Yang et al., 2022), as follows

$$h = \frac{b_0}{\langle(\boldsymbol{\alpha} - \boldsymbol{\alpha}_{\text{in}}) : \mathbf{n}\rangle} \exp\left[\frac{\mu_0}{\|\boldsymbol{\alpha}_{\text{in}}\|^u + \varepsilon}\left(\frac{b^M}{b_{ref}}\right)^w\right] \underbrace{\exp(k_3 A)}_{\textbf{fabric dependent}} \tag{28}$$

in which

$$b_0 = G_0 h_0 g(\theta)^{-n_g}(1 - c_h e)(p'/p_a)^{-0.5} \tag{29}$$

$$b^M = \left(\boldsymbol{\alpha}_\theta^M - \boldsymbol{\alpha}\right) : \mathbf{n} \tag{30}$$

$$b_{\text{ref}} = \left(\boldsymbol{\alpha}_\theta^B - \boldsymbol{\alpha}_{\theta+\pi}^B\right) : \mathbf{n} \tag{31}$$

In Eq. (28), $\boldsymbol{\alpha}_{\text{in}}$ is the value of $\boldsymbol{\alpha}$ at the initiation of a new loading process as explained in Dafalias and Manzari (2004). h_0, c_h, μ_0, u, ε and w are material constants, with the latter two having default values of ε=0.01 and w=2 as suggested by Yang et al. (2023). The new term $\exp(k_3 A)$ with a nonnegative material constant k_3 is introduced to phenomenologically describe a stiffer high-cycle response at higher A (e.g., smaller β_0 under TC), as observed experimentally in this study (see Fig. 2).

By substituting Eq. (28) into Eq. (17), the fabric-dependent plastic modulus K_p of the model can be derived, as below

$$K_p = \left(\frac{2}{3}\right) p' \frac{G_0 h_0 g(\theta)^{-n_g}(1 - c_h e)(p'/p_a)^{-0.5}}{\langle(\boldsymbol{\alpha} - \boldsymbol{\alpha}_{\text{in}}) : \mathbf{n}\rangle} \exp\left[\frac{\mu_0}{\|\boldsymbol{\alpha}_{\text{in}}\|^u + \varepsilon}\left(\frac{b^M}{b_{ref}}\right)^{w_1}\right] \exp(k_3 A)\left(\boldsymbol{\alpha}_\theta^B - \boldsymbol{\alpha}\right) : \mathbf{n} \tag{32}$$

The plastic modulus K_p, which is a key ingredient controlling cyclic shakedown/ratcheting, is enhanced to consider fabric anisotropy and its evolution through the memory and bounding surfaces in the SANISAND-FMSf model.

3.7. Reduction of stiffness and dilatancy in semifludised state

To capture the large shear strain development in the case of the post-liquefaction stage when soil exhibits "semifluidised state", an internal state variable named strain liquefaction factor l is introduced into the model (Barrero et al., 2019; Yang et al., 2022). The variable l is specifically formulated to operate only in the post-liquefaction stage (at a small mean effective

stress) for decreasing stiffness and dilatancy, without affecting the response in the pre-liquefaction state, as follows

$$\mathrm{d}l = \langle L \rangle [c_l \langle 1 - p_\mathrm{r}' \rangle (1 - l)^{n_l}] - c_\mathrm{r} l |\mathrm{d}\varepsilon_v| \quad (33)$$

In the first term of the RHS in Eq. (33), c_l and n_l are two positive model constants controlling the rate and the nonlinearity of l that evolves towards the unity, respectively. The pressure ratio $p_\mathrm{r}'=p'/p_\mathrm{th}'$ determines if the stress state falls within the semifluidised state, where p_th is a threshold mean effective stress (10 kPa by default). The form $\langle 1 - p_\mathrm{r}' \rangle$ enables this first term to only operate at small mean effective stress ($p_\mathrm{r}'< 1$) in the post-liquefaction stage. The second term of the RHS in Eq. (33) remains zero during undrained loading (i.e., $\mathrm{d}\varepsilon_v=0$), and renders l to evolve towards zero under drained loading with a model constant c_r controlling the evolution rate. Detailed explanations and quantitative investigation of Eq. (33) can be referred to Barrero et al. (2019) and Yang et al. (2022).

The evolving l is then incorporated into the model for decreasing the stiffness and dilatancy in the post-liquefaction stage. This is rendered by reducing the values of the hardening parameter h_0 and dilatancy parameter A_0 via the following two equations (Barrero et al., 2019)

$$h_0 = h_0' \{ [1 - \langle 1 - p_\mathrm{r}' \rangle]^{xl} + f_l \} \quad (34)$$

$$A_0 = A_0' \{ [1 - \langle 1 - p_\mathrm{r}' \rangle]^{xl} + f_l \} \quad (35)$$

where x and f_l are two model constants, with the latter having a default value of 0.01. In the post-liquefaction stage ($p_\mathrm{r}'< 1$), Eqs. (34) and (35) allow the values of h_0 and A_0 to decrease from the pre-defined material constants h_0' and A_0', rendering lower stiffness and less dilative response. In the pre-liquefaction stage ($p_\mathrm{r}'> 1$), Eqs. (34) and (35) lead to $h_0 = h_0'(1 + f_l)$ and $A_0 = A_0'(1 + f_l)$, which are almost identical to the predefined material constants h_0' and A_0' due to the very small value of f_l=0.01.

3.8. Stress-strain relationship

The plastic multiplier L can be calculated according to the stress increment $d\boldsymbol{\sigma}$ and plastic modulus K_p following the consistency equation, as first derived by Manzari and Dafalias (1997) and Dafalias and Manzari (2004)

$$L = \frac{1}{K_p}\frac{\partial f}{\partial \boldsymbol{\sigma}}:\mathrm{d}\boldsymbol{\sigma} = \frac{1}{K_p}p'\mathbf{n}:\mathrm{d}\mathbf{r} = \frac{1}{K_p}[\mathbf{n}:d\mathbf{s} - \mathbf{n}:\mathbf{r}\mathrm{d}p'] = \frac{2G\mathbf{n}:\mathrm{d}\mathbf{e} - K\mathbf{n}:\mathbf{r}\mathrm{d}\varepsilon_{\mathrm{v}}}{K_p + \frac{\partial f}{\partial \boldsymbol{\sigma}}:\mathbf{E}^e:\left(\mathbf{R}^* + \frac{D}{3}\mathbf{I}\right)} = \frac{2G\mathbf{n}:d\mathbf{e} - K\mathbf{n}:\mathbf{r}\mathrm{d}\varepsilon_{\mathrm{v}}}{K_p + 2G(\mathbf{n}:\mathbf{R}^*) - KD\mathbf{n}:\mathbf{r}} \tag{36}$$

The elastoplastic stress-strain relationship can be expressed as

$$\mathrm{d}\boldsymbol{\sigma} = 2G\mathrm{d}\mathbf{e} + K\mathrm{d}\varepsilon_v\mathbf{I} - \langle L\rangle\{2G\mathbf{R}^* + KD\mathbf{I}\} \tag{37}$$

A complete summary of the equations for the SANISAND-FMSf model is given in Table 2.

3.9. Determination of model constants

The model constants of the proposed high-cycle anisotropic model are summarized in Table 4. The new model consists of 28 material constants, with 7 of them having default values, as marked in Table 2. The remaining 21 constants that require calibration can be divided into three groups.

The first group is related to 16 constants inherited from SANISAND (Dafalias and Manzari, 2004), for which the calibration procedures are given in detail by Taiebat et al. (2010). The second group includes 5 constants inherited from the formulations for stiffness and dilatancy degradation in semifludised state, with their calibration procedures described by Barrero et al. (2019) and Yang et al. (2022). These two groups of constants can be calibrated against tests on specimens with similar initial fabric anisotropy.

The last group of model constants are associated with the initial value and evolution rate of fabric anisotropy (F_0 and k_{f}), and the influence of fabric on dilatancy (e_{A}, k_1), isotropic hardening of MS (k_2) and kinematic hardening of BS (k_3). It is found that the variation of F_0 and k_{f} are relatively small for the three sands concerned in this study, which only need to be fine-tuned within narrow ranges of F_0=0.3-0.5 and k_{f}=5.0-8.0, respectively. The model constant e_{A} can be determined by trial-and-error to fit the monotonic results from triaxial compression and triaxial extension tests. The constants k_1, k_2 and k_3 can be fine-tuned based on cyclic tests considering different initial fabric anisotropy of sand.

552 **Table 2**

553 **Constitutive equations and model constants**

Features.	Equations	Parameters
Elasticity	$G = G_0\,(2.97-e)^2/(1+e)\sqrt{p' p_{\mathrm{a}}}$ $K = 2G(1+\nu)/[3(1-2\nu)]$	G_0 ν
Fabric evolution	$\mathrm{d}\mathbf{F} = \langle L\rangle k_{\mathrm{f}}(\mathbf{R}^*/\parallel \mathbf{R}^* \parallel - \mathbf{F})e^{\mathrm{A}}$	k_{f}
Critical state line	$e_{\mathrm{c}} = e_{\Gamma} - \lambda_{\mathrm{c}}(p'/p_{\mathrm{a}})^{\xi}$ $\zeta = \psi - e_{\mathrm{A}}(A-1)$ $A = \mathbf{F}\colon(\mathbf{R}^*/\parallel \mathbf{R}^* \parallel)$	$e_{\Gamma},\ \lambda_{\mathrm{c}}, \xi$ e_{A}
Yield surface	$f = \sqrt{(\mathbf{s}-p'\boldsymbol{\alpha})\colon(\boldsymbol{s}-p'\boldsymbol{\alpha})} - \sqrt{2/3}\,p' m$=0	$m =$ 0.01
Memory surface	$f^{\mathrm{M}} = \sqrt{(\alpha_\theta^M - \alpha^M)\colon(\alpha_\theta^M - \alpha^M)} - \sqrt{2/3}\,m^{\mathrm{M}}$=0	m^{M}
Plastic hardening	$\mathrm{d}\boldsymbol{\alpha} = 2/3\,\langle L\rangle h(\boldsymbol{\alpha}_\theta^{\mathrm{B}} - \boldsymbol{\alpha})$; $K_{\mathrm{p}} = 2/3\,p' h(\boldsymbol{\alpha}_\theta^{\mathrm{B}} - \boldsymbol{\alpha})\colon\mathbf{n}$ $h = \dfrac{G_0 h_0 g(\theta)^{-n_{\mathrm{g}}}(1-c_{\mathrm{h}}e)(p'/p_{\mathrm{a}})^{-0.5}}{\langle(\boldsymbol{\alpha}-\boldsymbol{\alpha}_{\mathrm{in}})\colon\mathbf{n}\rangle}\exp\left[\dfrac{\mu_0}{\|\boldsymbol{\alpha}_{\mathrm{in}}\|^u + \varepsilon}\left(\dfrac{b^M}{b_{ref}}\right)^w\right]\exp(k_3 A)$ $b^{\mathrm{M}} = (\boldsymbol{\alpha}_\theta^{\mathrm{M}} - \boldsymbol{\alpha})\colon\mathbf{n}$; $b_{\mathrm{ref}} = (\boldsymbol{\alpha}_\theta^{\mathrm{B}} - \boldsymbol{\alpha}_{\theta+\pi}^{\mathrm{B}})\colon\mathbf{n}$ $L = (1/K_p)\,\partial f/\partial\boldsymbol{\sigma}\colon d\boldsymbol{\sigma}$ $\boldsymbol{\alpha}_\theta^{\mathrm{B}}$=$\sqrt{2/3}\,[g(\theta)M\exp(-n^b\zeta) - m]\mathbf{n}$	μ_0, u $w = 2$, $\varepsilon = 0.01,\ k_3$
Memory surface evolution	$\mathrm{d}m^{\mathrm{M}} = \langle L\rangle\left\{\sqrt{3/2}\ c_c h^{\mathrm{M}}\langle(\boldsymbol{\alpha}_\theta^{\mathrm{B}} - \boldsymbol{\alpha}_\theta^{\mathrm{M}})\colon\mathbf{n}\rangle\underbrace{\exp[-k_2(1-A)]}_{\textbf{fabric dependent}} - \dfrac{m^{\mathrm{M}}}{\varsigma}\left|(\boldsymbol{\alpha}_\theta^{\mathrm{B}} - \boldsymbol{\alpha}_\theta^{\mathrm{M}})\colon\mathbf{n}\right|\langle -D\rangle\right\}$ $\mathrm{d}\boldsymbol{\alpha}^{\mathrm{M}} = 2/3\,\langle L\rangle h^M(\boldsymbol{\alpha}_\theta^{\mathrm{B}} - \boldsymbol{\alpha}_\theta^{\mathrm{M}})$ $h^M = \dfrac{1}{1 + c_c\mathcal{H}\left[\left((\boldsymbol{\alpha}_\theta^{\mathrm{B}} - \boldsymbol{\alpha}_\theta^{\mathrm{M}})\right)\colon\mathbf{n}\right]\underbrace{\exp[-k_2(1-A)]}_{\textbf{fabric dependent}}}\left[h + \sqrt{3/2}\dfrac{m^M \mathrm{sgn}\left[\left((\boldsymbol{\alpha}_\theta^{\mathrm{B}} - \boldsymbol{\alpha}_\theta^{\mathrm{M}})\right)\colon\mathbf{n}\right]\langle -D\rangle}{\varsigma}\right]$ $\boldsymbol{\alpha}_\theta^{\mathrm{M}} = \boldsymbol{\alpha}^{\mathrm{M}} + \sqrt{2/3}\,m^{\mathrm{M}}\mathbf{n}$	$c_c = 1$ $k_2,\ \varsigma$=0.00001
Plastic deviatoric strain increment	$\mathrm{d}\mathbf{e}^{\mathrm{p}} = \langle L\rangle\mathbf{R}^*$ $\mathbf{R}^* = \left(\dfrac{\langle\|\boldsymbol{\alpha}_{\theta_\alpha}^{\mathrm{B}}\| - \|\boldsymbol{\alpha}\|\rangle}{\|\boldsymbol{\alpha}_{\theta_\alpha}^{\mathrm{B}}\|}\right)^2\mathbf{n} + \left[1 - \left(\dfrac{\langle\|\boldsymbol{\alpha}_{\theta_\alpha}^{\mathrm{B}}\| - \|\boldsymbol{\alpha}\|\rangle}{\|\boldsymbol{\alpha}_{\theta_\alpha}^{\mathrm{B}}\|}\right)^2\right]\dfrac{\mathbf{R}'}{\|\mathbf{R}'\|}$ $\mathbf{R}' = B\mathbf{n} - C[\mathbf{n}^2 - \mathbf{I}/3]$	
Plastic volumetric strain increment	$\mathrm{d}\varepsilon_{\mathrm{v}}^{\mathrm{p}} = \langle L\rangle D$ $D = \{A_0 g(\theta)^{-n_{\mathrm{g}}}(1 + \langle\mathbf{z}\colon\mathbf{n}\rangle)(\boldsymbol{\alpha}_\theta^{\mathrm{D}} - \boldsymbol{\alpha})\colon\mathbf{n}\}\underbrace{\exp[k_1(1-A)]}_{\textbf{fabric dependent}}$ $\mathrm{d}\mathbf{z} = -c_z\langle -\mathrm{d}\varepsilon_{\mathrm{v}}^{\mathrm{p}}\rangle(z_{max}\mathbf{n} + \mathbf{z})$ $\boldsymbol{\alpha}_\theta^{\mathrm{D}} = \sqrt{2/3}\,[g(\theta)M\exp(n^{\mathrm{d}}\zeta) - m]\mathbf{n}$	A_0, n_{g}, k_1 c_z, z_{max},
Strain liquefaction factor rate	$\mathrm{d}l = \langle L\rangle[c_l\langle 1 - p_{\mathrm{r}}'\rangle(1-l)^{n_l}] - c_{\mathrm{r}} l\,\mathrm{d}\varepsilon_v\,\mathrm{d}\varepsilon_v$ p_{r}'=p'/p_{th}' $h_0 = h_0'\{[1 - \langle 1 - p_{\mathrm{r}}'\rangle]^{xl} + f_l\}$ $A_0 = A_0'\{[1 - \langle 1 - p_{\mathrm{r}}'\rangle]^{xl} + f_l\}$	$c_l, n_l = 8$, c_{r}=0, p_{th}'=10 kPa, x, f_l=0.01

554 *Some constants have indicated default numerical values (m=0.01)

Table 3

Summary of the experiments for model validation

Sand type	Drainage condition	Cyclic characteristics	p_0' (kPa)	e_0	β_0	Reference
Fujian sand	Drained	One-way non-symmetrical	200	0.67-0.77	0°, 45°, 90°	This study
Toyoura sand	Drained	Two-way non-symmetrical	196	0.65-0.66	0°	Masaya et al., 2001
	Undrained	Two-way non-symmetrical	196	0.660-0.663	0°	Masaya et al., 2001
	Undrained	Two-way symmetrical	100	0.698	0°, 45°, 90°	Oda et al., 2001
Karlsruhe fine sand	Drained	One-way 1D compression	1-1000	0.756-0.997	0°	Wichtmann and Triantafyllidis 2016a
	Undrained	One-way non-symmetrical	200	0.80-0.82	0°	Wichtmann and Triantafyllidis 2016b
	Undrained	Two-way symmetrical	100-300	0.79-0.83	0°	Wichtmann and Triantafyllidis 2016b
	Undrained	Two-way non-symmetrical	200	0.69-0.95	0°	Wichtmann and Triantafyllidis 2016b

4. Model validation and predictions

Section 4.1 and Section 4.2, respectively, present model validations against experiments performed in this study and reported in the literature, which cover a wide range of states (including density, stress level and fabric anisotropy), cyclic amplitudes, stress paths and drainage conditions. The experimental conditions are summarized in Table 3 while their model constants are presented in Table 4.

4.1. Validation against experiments performed in this study: high-cycle drained triaxial compression tests

According to Table 1, nine stress-controlled high-cycle simulations of the anisotropic granular soil were performed in this study. The simulated cyclic stress-strain relationships are presented in Figs. 2b, for comparison with experimental results in Figs. 2a. The simulated high-cycle accumulations of axial and volumetric strain under different conditions are shown in Fig. 3-5, for comparisons with their experimental counterparts, as illustrated in the same figures.

The above comparisons suggest the SANISAND-FMSf model is capable of quantitatively reproducing various drained high cycle deviatoric and volumetric strains of anisotropic granular soil with a unified set of model constants. Meanwhile, the SANISAND-FMSf model can

573 **Table 4**

574 **Model constants for three types of sands**

Parameter	Symbol	Fujian sand	Toyoura sand	Karlsruhe sand
Elastic modulus	G_0	125	125	100
	ν	0.05	0.05	0.05
Critical state line	M_c	1.35	1.25	1.28
	c	0.75	0.712	0.75
	e_Γ	1.135	0.934	1.038
	λ_c	0.055	0.019	0.056
	ξ	0.7	0.7	0.28
Yield surface	m	0.01	0.01	0.01
	n_g	0.95	0.9	0.95
Hardening parameters	h_0'	5.6	9.0	7.6
	c_h	1.01	0.968	1.015
	n^b	1.2	1.25	1.0
	k_3	0.1	0.05	0.03
Dilatancy parameters	n^d	1.6	0.7	1.2
	e_A	0.095	0.095	0.015
	A_0'	0.7	0.4	0.56
	z_{max}	5	5	15
	c_z	500	800	1000
	k_1	0.2	0.1	0.05
Fabric anisotropy and evolution	k_f	5.8	5.0	5.8
	F_0	0.45	0.3	0.35
Memory surface evolution	μ_0	10	8	7.8
	u	0.3	0.87	0.87
	ς	0.00001	0.00001	0.00001
	k_2	0.005	0.0005	0.001
Semifluidised state	c_l	10	10	25
	x	3.5	5.5	3.3
	c_r	0	0	0
	n_l	8	8	8
	f_l	0.01	0.01	0.01

575

capture the following key experimental observations:

1. gradual soil stiffening with reducing plastic dissipation for all specimens under high-cycle loading;
2. a transition from cyclic shakedown to ratcheting, by solely deviating the major fabric orientation of relatively dense specimens from their loading direction (increasing β_0);
3. cyclic ratcheting for relatively loose specimens with different fabric orientations, under a medium cyclic stress amplitude;
4. cyclic shakedown for relatively loose specimens with different fabric orientations, under a low cyclic stress amplitude.

The unique feature of the model lies in its capability to capture the distinct high-cycle strain accumulation responses (shakedown or ratcheting) at varied fabric anisotropy. This is mainly attributed to the novel features of the SANISAND-FMSf model, which links the fabric-related micro-structure evolution to K_p through the memory and bounding surfaces. Further elaborations are given in Fig. 8, to show how the proposed model works for the experiments

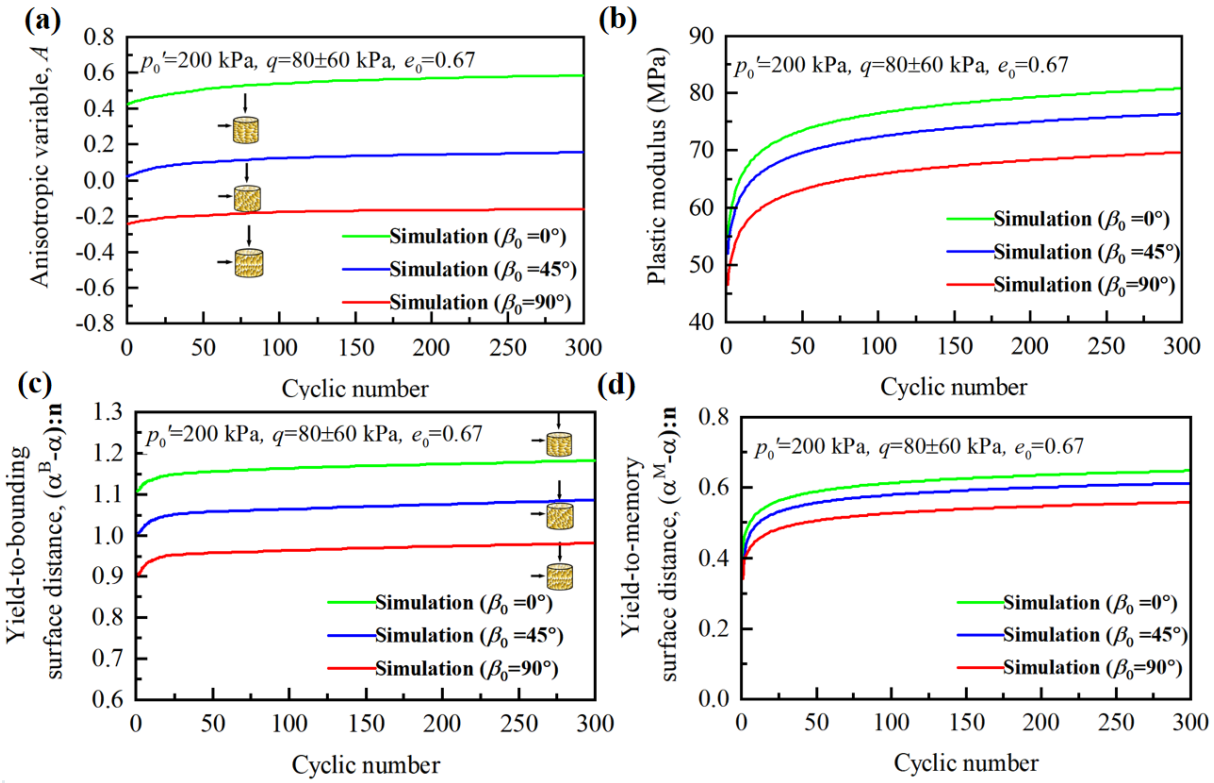

Fig. 8. Evolution of fabric-related variables with the number of cycles under different initial bedding plane angles (bedding angle β_0=0°, 45° and 90°), with simulation settings as p_0'=200 kPa, q=80±60 kPa, e_0=0.67: (a) anisotropic variable A. (b) yield-to-memory surface distance $(\boldsymbol{\alpha}^{\mathbf{M}}-\boldsymbol{\alpha}):\mathbf{n}$. (c) yield-to-bounding surface distance $(\boldsymbol{\alpha}^{\mathbf{B}}-\boldsymbol{\alpha}):\mathbf{n}$. (d) plastic modulus K_p.

presented in Fig. 3. As β_0 increases, the model gives a lower A that evolves more slowly under cyclic loading, rendering smaller yield-to-memory surface distance $(\boldsymbol{\alpha}^{\mathrm{M}}-\boldsymbol{\alpha}):\mathbf{n}$ and shorter yield-to-bounding surface distance $(\boldsymbol{\alpha}^{\mathrm{B}}-\boldsymbol{\alpha}):\mathbf{n}$, and thus a lower K_{p} [see Eq. (34)]. Consequently, a high-cycle loaded specimen with a higher β_0 is more prone to ratcheting, rather than shakedown. Meanwhile, the consideration of fabric evolution that enhances K_{p} has naturally enabled the model to simulate soil stiffening with smaller hysteresis loops, which are not captured by the platform model SANISAND (Dafalias and Manzari, 2004).

Despite the reasonable predictions for high-cycle strain accumulations, which is the primary feature as intended in the SANISAND-FMSf model of its present version, the unloading and reloading stiffness is not properly captured for all the cases (Fig. 2). Future work is needed to improve the predictive ability for the stiffness in this regard by introducing additional constitutive ingredients in the proposed model, such as non-linearity of soil stiffness at small strains.

4.2. Validation against experiment of different loading types

Given the limited datasets on Fujian sand that hinders a comprehensive model validation (as presented in Section 4.1), this section further validates the model against various cyclic tests on two typical sands, i.e., Karlsruhe fine sand ($e_{\max}$=1.054, $e_{\min}$=0.677) and Toyoura sand ($e_{\max}$=0.972, $e_{\min}$=0.609). The datasets of Karlsruhe fine sand were reported by Wichtmann and Triantafyllidis (2016a, b), consisting of 16 cyclic tests which cover: (a) a wide range of initial states (isotropically- and anisotropically-consolidated specimens with e_0=0.69-0.997, p_0'=100-1000 kPa), and (b) various loading types (1D compression, triaxial compression and extension with symmetrical and non-symmetrical loading) under drained and undrained conditions. The experimental data of Toyoura sand were reported by Masaya et al. (2001) and Oda et al. (2001), including 10 cyclic tests with a wide range of initial states (β_0=0°-90°, e_0 =0.65-0.698) and multiple loading types (triaxial compression and extension with symmetrical and non-symmetrical loading) under both drained and undrained conditions.

4.2.1. Drained cyclic oedometer tests under one-way loading

The experimental data of volumetric behavior under drained cyclic oedometer tests on Karlsruhe fine sand from Wichtmann and Triantafyllidis (2016a) are simulated by the

SANISAND-FMSf model. Four specimens were tested, including the loose (initial void ratio e_0=0.997), medium dense (e_0=0.888) and dense specimens (e_0=0.791 and 0.756). For each specimen, four loading cycles with increasing maximum vertical stress (20, 55, 145 and 405 kPa) were imposed as shown in Fig. 9.

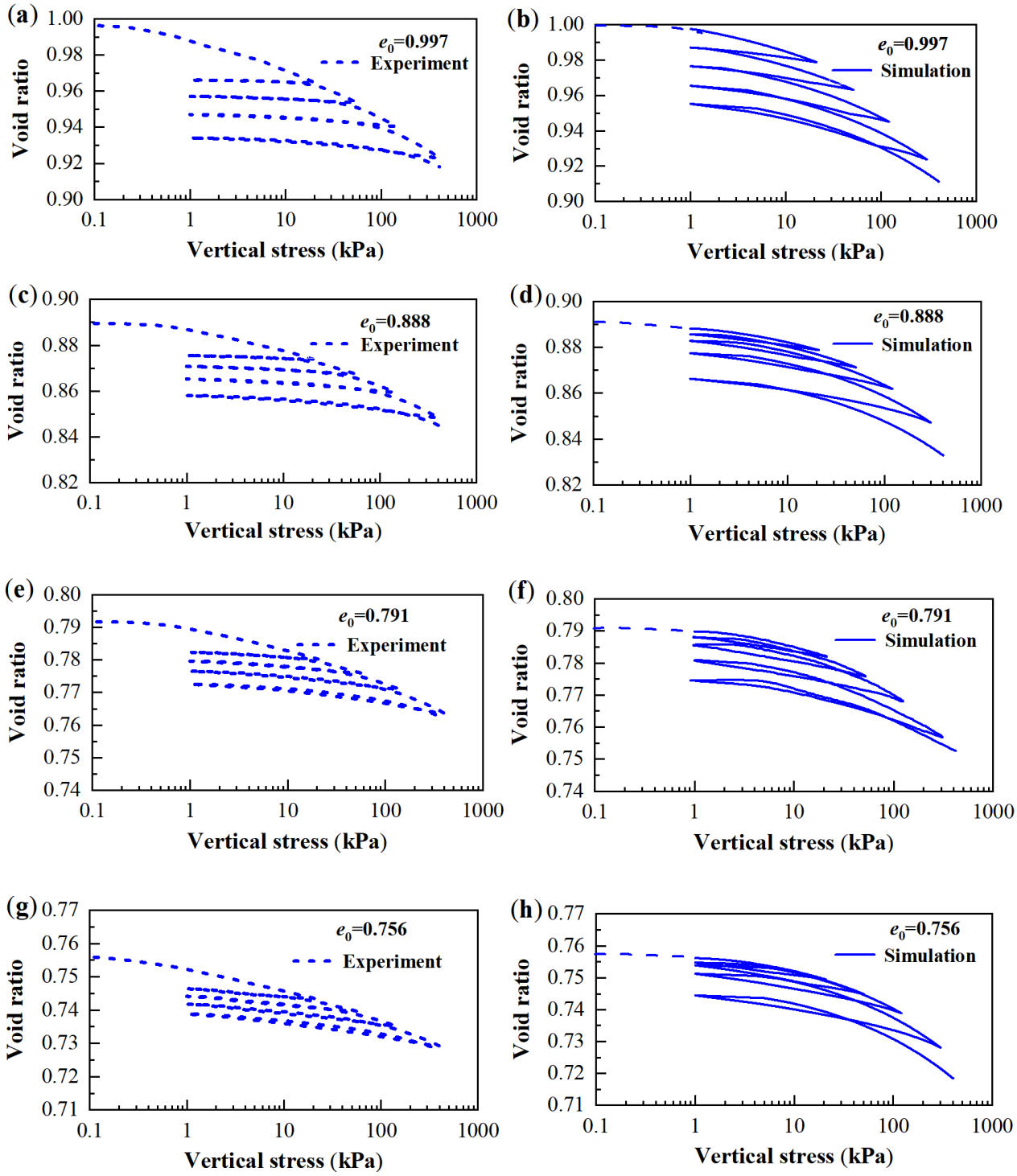

Fig. 9. Simulations compared with experiments in drained cyclic oedometer tests under one-way loading on Karlsruhe fine sand with different e_0 (i.e., 0.997, 0.888, 0.791 and 0.756): (a), (c), (e) and (g) experimental data from Wichtmann and Triantafyllidis (2016a); (b), (d), (f) and (h) simulations by the proposed model.

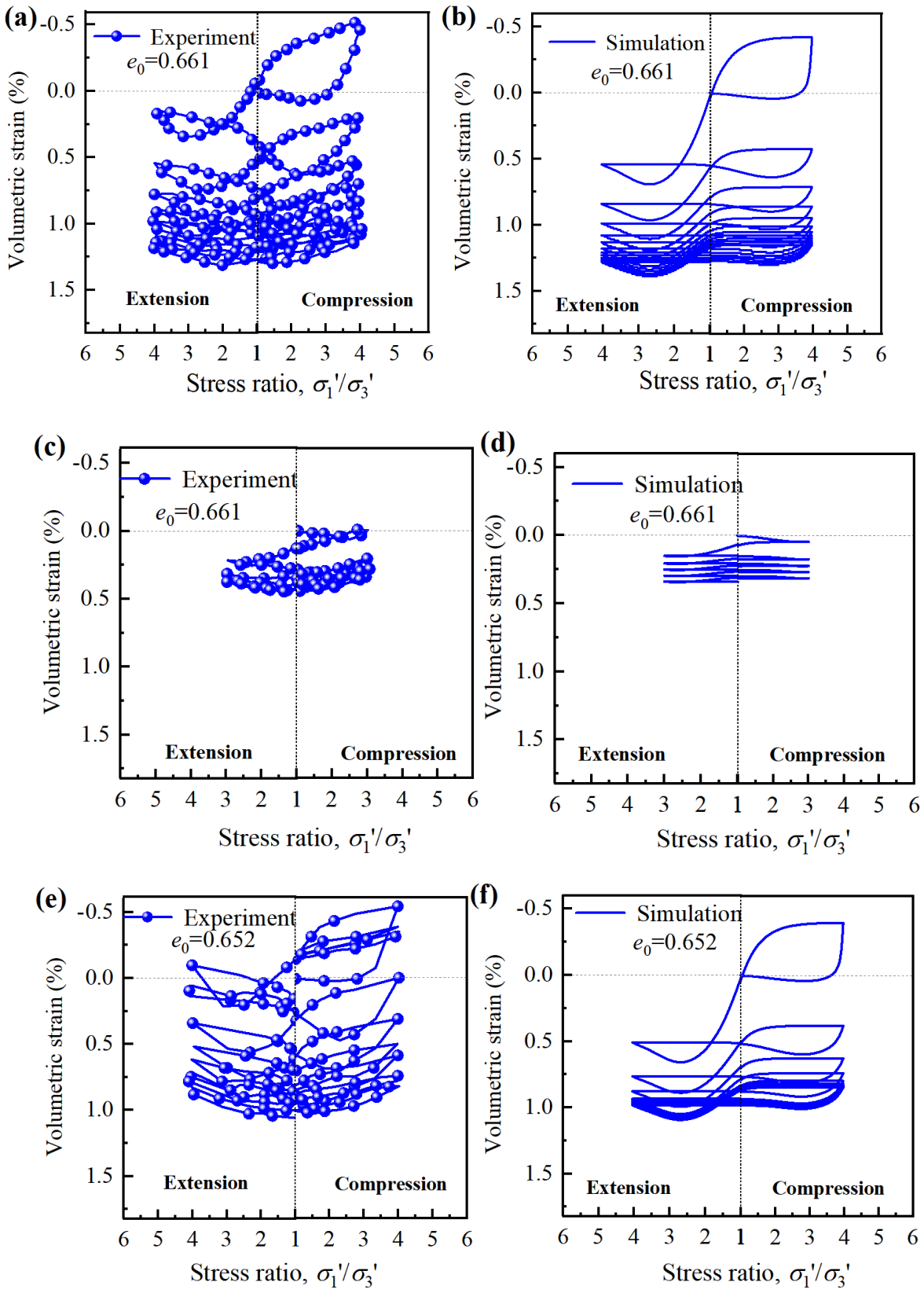

Fig. 10. Simulations compared with experiments in constant p' cyclic drained triaxial tests under two-way non-symmetrical loading on Toyoura sand with different e_0 (i.e., 0.661 and 0.652): (a), (c) and (e) experimental data from Masaya et al. (2001); (b), (d) and (f) simulations by the proposed model.

Fig. 9 shows the model broadly captures the evolution trends of void ratio during the cyclic compression of the four experiments, i.e. looser specimens contract more than denser ones

under each given cyclic amplitude. It is worth noting that the model underestimates the volumetric compression during the first monotonic loading stage for the four specimens with different densities. This is likely attributed to the ignorance of $d\varepsilon_v^p$ at a constant stress ratio η by the SANISAND-FMSf model. By introducing the capped yield surface (Taiebat and Dafalias, 2008), the prediction of the cyclic oedometer response could be improved. It can also be seen that the simulated unloading stiffness is smaller than the measured one, particularly at the onset of each unloading stage. This could be improved by incorporating the path-dependent stiffness at small strains (Niemunis and Herle, 1997).

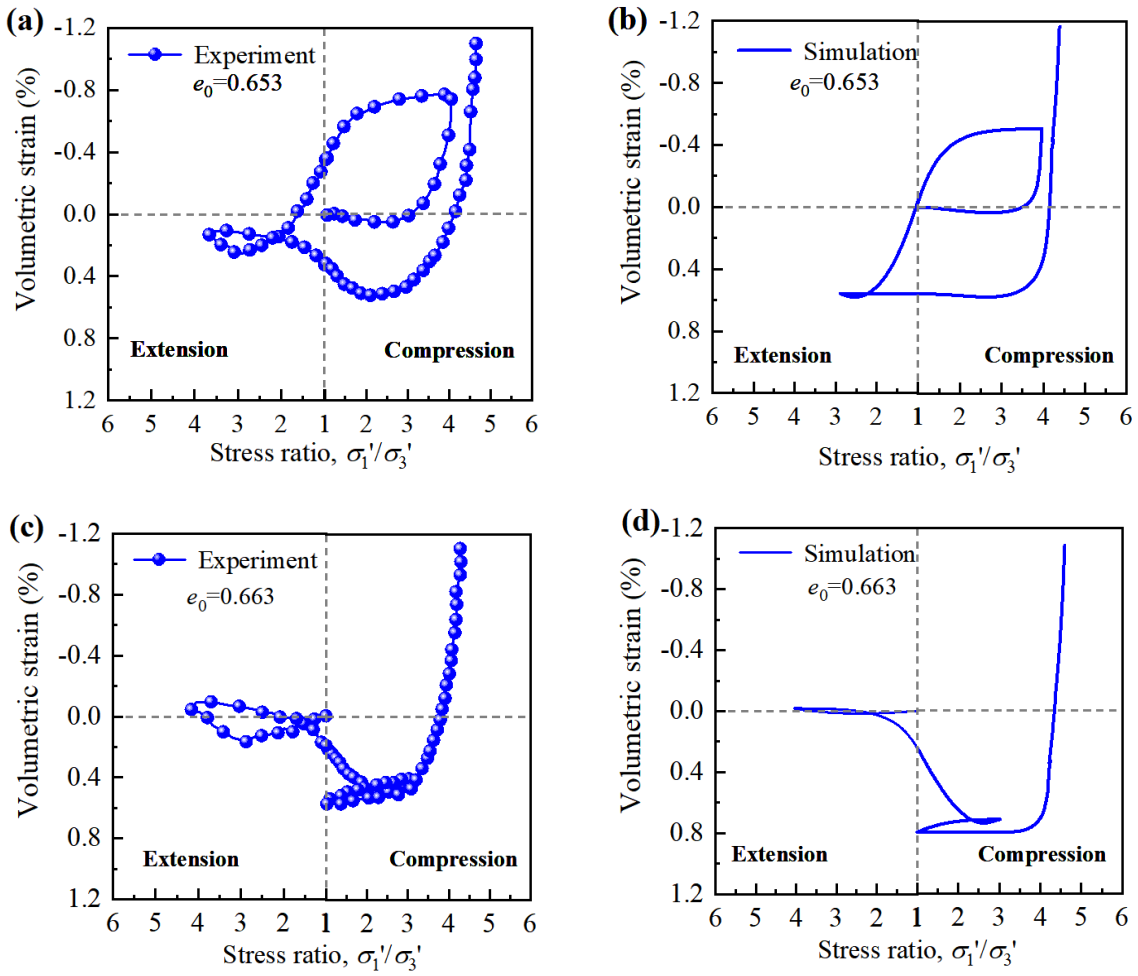

Fig. 11. Comparison between simulations and experiments of the volumetric strain in constant p' cyclic drained triaxial tests under two-way non-symmetrical loading on Toyoura sand with different e_0 (i.e., 0.653 and 0.663): (a), (c) and (e) experimental data from Masaya et al. (2001); (b), (d) and (f) simulations by the proposed model.

4.2.2. Drained cyclic triaxial tests under two-way non-symmetrical loading

Fig. 10 compares the measured and simulated volumetric strain accumulation of Toyoura sand in drained cyclic triaxial tests at constant p'=196 kPa under two-way non-symmetrical

loading. Two different stress ratios σ_1'/σ_3' (i.e., 3 and 4) and e_0 (i.e., 0.661 and 0.652) were considered in these experiments (Masaya et al., 2001). The model reasonably predicts the transitions between contraction and dilation during the cyclic loading, and the trend towards a shakedown response as the sand densifies. It quantitatively captures the experimentally observed larger volumetric strain due to higher σ_1'/σ_3' or larger e_0 under otherwise identical conditions. This is mainly owing to the use of the evolving dilatancy tensor **z** in the dilatancy expression, as proposed by Dafalias and Manzari (2004). With the same set of model constants, the model quantitatively reproduces the volumetric and stress-strain responses subjected to different loading types (i.e., load, unload and reload until failure) on the same sand with variable e_0 (i.e., 0.653 and 0.663), as illustrated in Figs. 11-12.

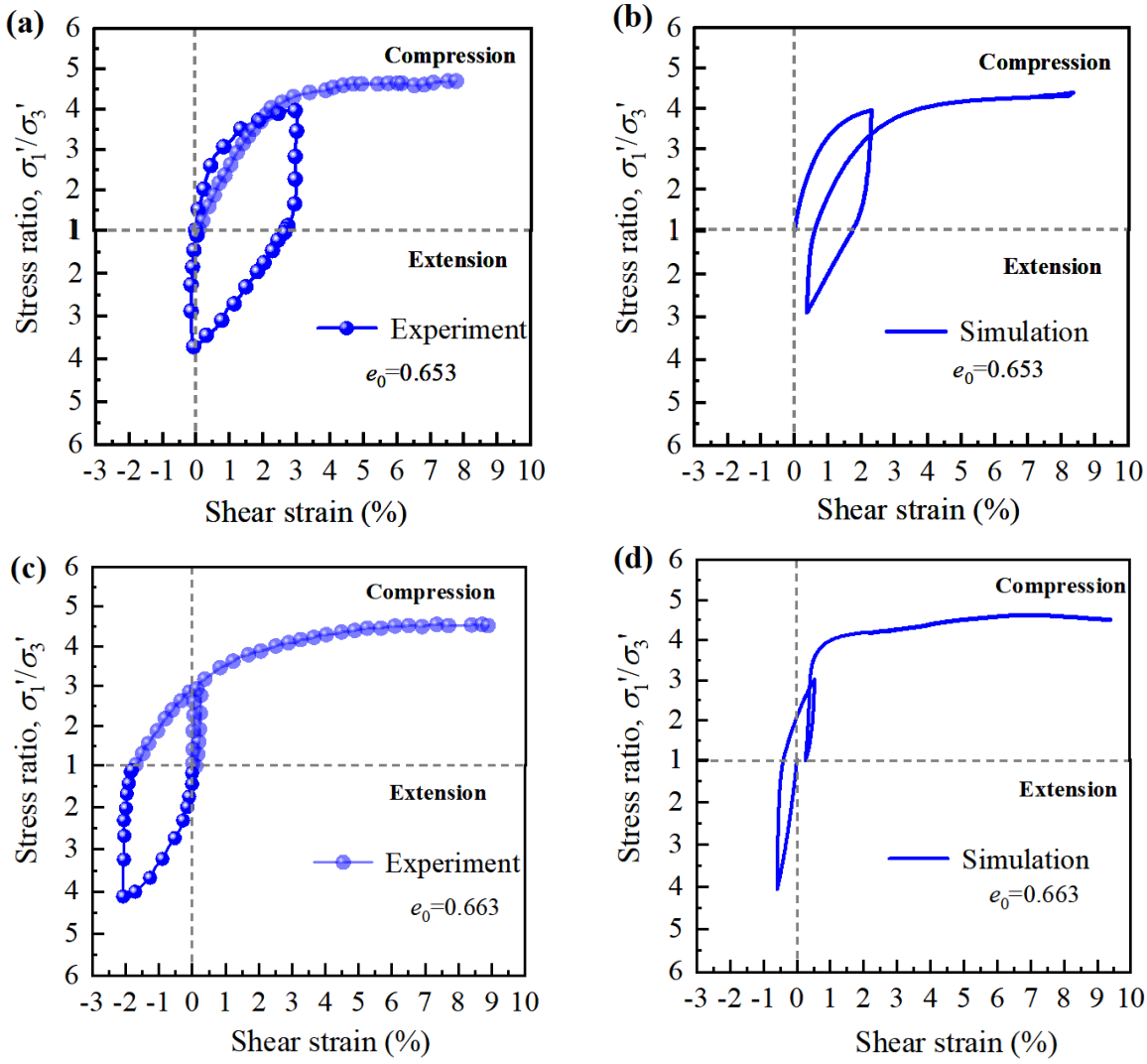

Fig. 12. Comparison between simulations and experiments of the shear strain in constant p' cyclic drained triaxial tests under two-way non-symmetrical loading on Toyoura sand with different e_0 (i.e., 0.653 and 0.663): (a), (c) and (e) experimental data from Masaya et al. (2001); (b), (d) and (f) simulations by the proposed model.

4.2.3. High-cycle undrained triaxial tests under two-way symmetrical loading

Having validated the model against drained cyclic experiments, this sub-section and the subsequent two sub-sections aim to validate its simulation abilities for capturing the undrained cyclic behavior of Karlsruhe fine sand and Toyoura sand under different loading types. Figs. 13-14 and Figs. 15-16, respectively, show the comparisons between the measured and simulated results of undrained triaxial tests on Karlsruhe fine sand under symmetrical loading with different cyclic stress ratios CSR=q_{amp}/p_0' (i.e., 0.2, 0.25 and 0.3) and different initial void ratios (i.e., 0.83 and 0.79). In general, the model reasonably reproduces the influences of cyclic loading amplitude and void ratio on the undrained responses of the given sand. Particularly, it captures the small amplitude of strain accumulation under high-cycle loading (e.g., over 200 cycles for the low CSR=0.2) in the pre-liquefaction stage, as well as the large strain development in the post-liquefaction stage. The reproduction of these features, which are

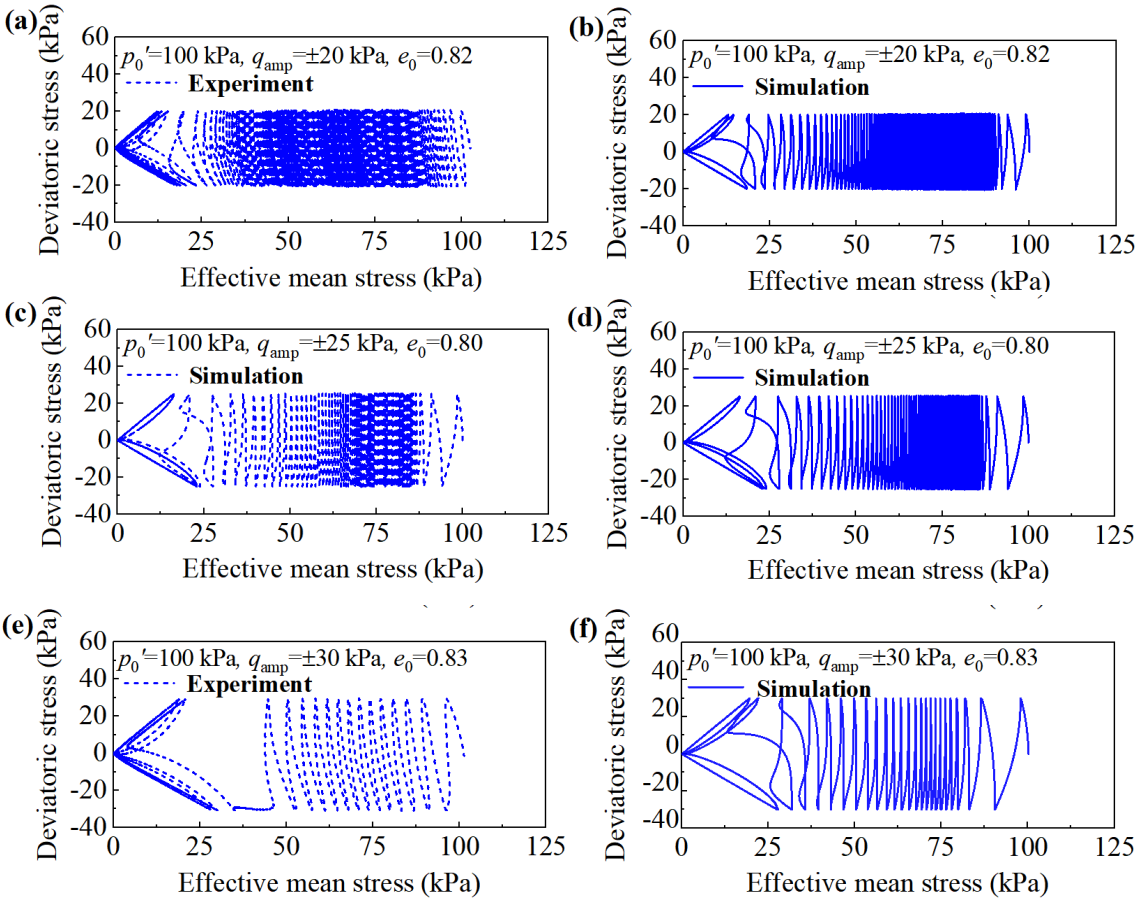

Fig. 13. Comparison between simulations and experiments of the stress path in two-way symmetrical undrained cyclic triaxial tests on Karlsruhe fine sand with different CSR (i.e., 0.2, 0.25 and 0.3): (a), (c) and (e) experimental data from Wichtmann and Triantafyllidis (2016b); (b), (d) and (f) simulations by the proposed model.

intended but not always captured by the existing models, is mainly attributed to the constitutive ingredients of MS and semifluidised state. It is also worth noting that the model quantitatively captures the experimentally observed butterfly-shaped stress path during cyclic mobility, where the effective mean stress drops to nearly zero during each contraction process following dilation (upon stress reversal). This is mainly owing to the introduction of the evolving dilatancy tensor **z** in the dilatancy expression (Dafalias and Manzari, 2004), which has enhanced contraction following each stress reversal to facilitate the build-up of pore water pressure, causing reduction of effective stress to be nearly zero.

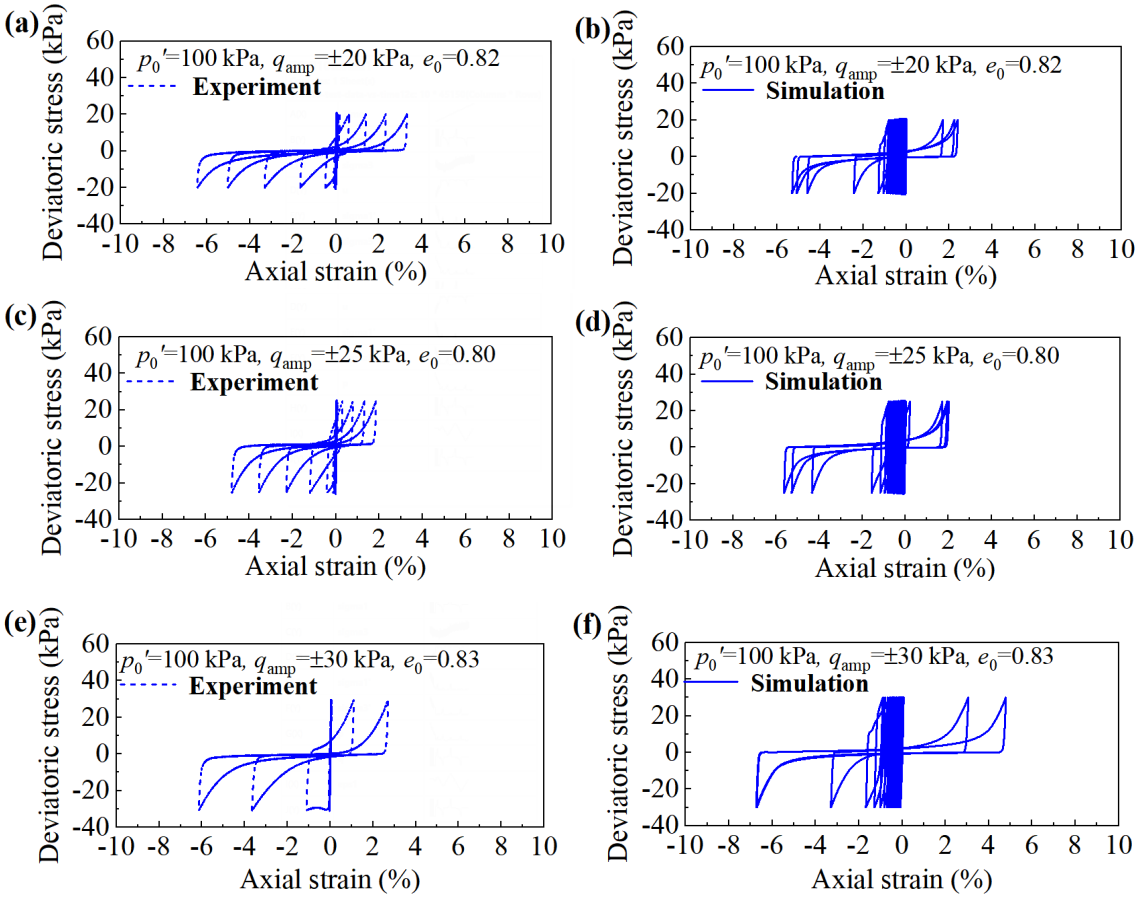

Fig. 14. Comparison between simulations and experiments of the stress-strain relations in two-way symmetrical undrained cyclic triaxial tests on Karlsruhe fine sand with different CSR (i.e., 0.2, 0.25 and 0.3): (a), (c) and (e) experimental data from Wichtmann and Triantafyllidis (2016b); (b), (d) and (f): simulations by the proposed model.

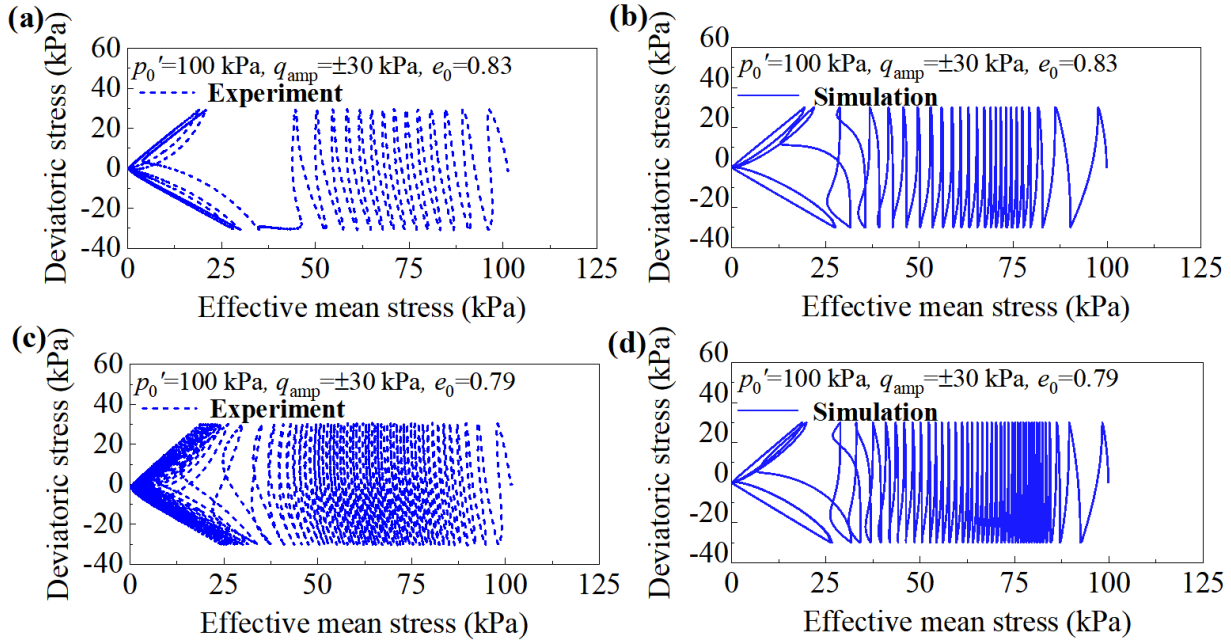

Fig. 15. Comparison between simulations and experiments of the stress path in two-way symmetrical undrained cyclic triaxial tests on Karlsruhe fine sand with different e_0 (i.e., 0.83 and 0.79): (a) and (c) experimental data from Wichtmann and Triantafyllidis (2016b); (b) and (d) simulations by the proposed model.

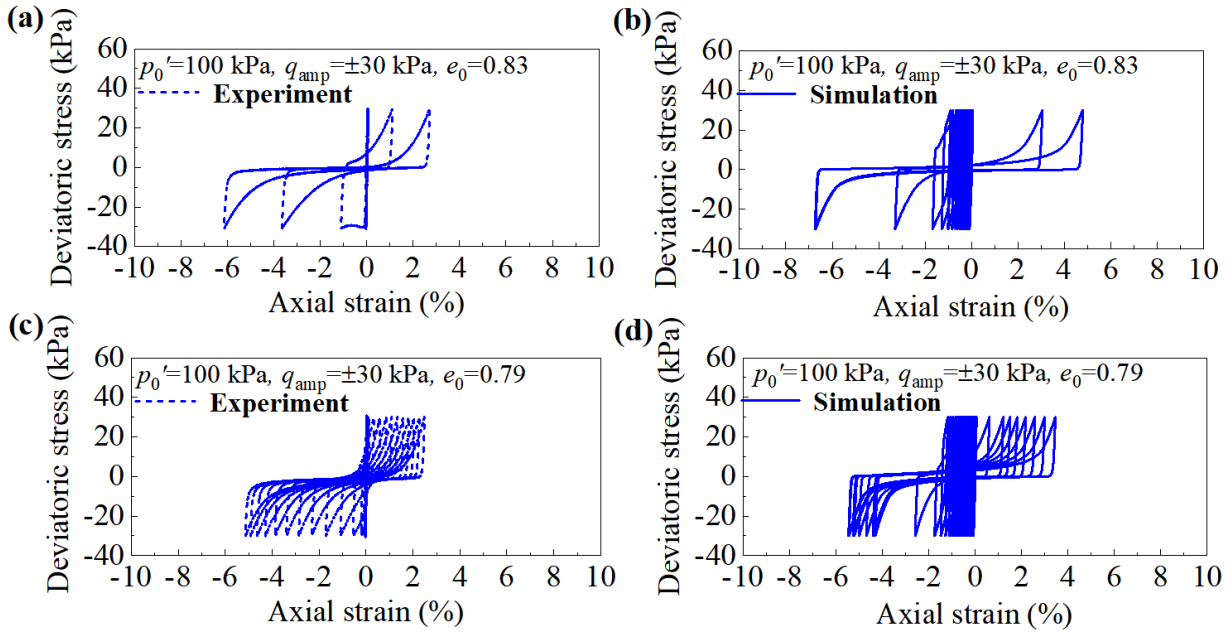

Fig. 16. Comparison between simulations and experiments of the stress-strain relations in two-way symmetrical undrained cyclic triaxial tests on Karlsruhe fine sand with different e_0 (i.e., 0.83 and 0.79): (a) and (c) experimental data from Wichtmann and Triantafyllidis (2016b); (b) and (d) simulations by the proposed model.

4.2.5. Undrained cyclic triaxial tests under two-way non-symmetrical loading

The model is further challenged to validate against cyclic undrained experiments of the two sands (Karlsruhe fine sand and Toyoura sand) under two-way non-symmetrically loading,

674 using the same sets of material constants given in Table 4. Figs. 17a and 17c and Figs. 18a
675 and18c, respectively, show the measured effective stress path and stress-strain relationship of
676 Karlsruhe fine sand under two-way non-symmetrical triaxial loading (Wichtmann and
677 Triantafyllidis, 2016b). For comparison, the measured data of Karlsruhe fine sand under one-
678 way cyclic loading are illustrated in Figs. 17e and 17g and Figs. 18e and 18g. In all the tests
679 shown in Figs. 17-18, the specimens are anisotropically consolidated to the same p_0'=200 kPa,
680 but at different q (i.e., -100, -50, 50 and 150 kPa), ending up with very similar e_0 (ranging
681 between and 0.80-0.84). The same cyclic amplitude q_{amp}=60 kPa was then imposed to these
682 specimens during the subsequent cyclic loading tests.

683 As shown in Figs. 17-18, the model simulations reasonably agree with the experimental
684 data, in terms of effective stress paths and modes of cyclic strain accumulation. It captures the
685 key experimental observations that for a given q_{ampl} and initial state (e_0, p_0'), the occurrence
686 of liquefaction depends on the average cyclic stress q_{ave}. Under relatively small q_{ave} that
687 causes two-way non-symmetrical loading (including compression-to-extension reversals),
688 cyclic mobility with p' approaching zero is triggered (Figs. 17b and 17d). Conversely, under
689 relatively high q_{ave} that leads to one-way loading (without compression-to-extension
690 reversals), no liquefaction is caused, with p' terminating at a point far higher than zero (Figs.
691 17f and 17h). It is worth noting that the model performs satisfactorily when the initial stress
692 ratio $\eta_{ini} = q_{ave}/p_0'$ is relatively small, i.e., $|\eta_{ini}|<$ 0.25 (Figs. 17 a-d). Under relatively
693 higher η_{ini} (i.e., $|\eta_{ini}| \geq$ 0.5, see Figs. 17 e-f), the simulated results do not agree well with
694 the experimental data. This appears to imply that the proposed model formulations may not
695 work well when strong initial stress anisotropy is involved. Improved simulation capability may
696 be achieved by incorporating the effect of initial stress anisotropy into some key constitutive
697 ingredients, e.g., dilatancy function, as exercised by Yang et al. (2018).

698 Fig. 19 shows the comparison between measured and simulated effective stress paths of
699 strain-controlled (cyclic strain amplitude=±1%) undrained cyclic triaxial tests on Karlsruhe fine
700 sand with different densities (e_0=0.95, 0.82 and 0.69). The measured and simulated stress-strain
701 relationships of these tests are illustrated in Fig. 20. The model shows a satisfactory
702 performance in reproducing both pre-liquefaction and post-liquefaction responses of the loose,
703 medium dense and dense specimens. This leads to further confirmation of the model's ability

to describe state-dependent cyclic responses of Karlsruhe fine sand under different loading types.

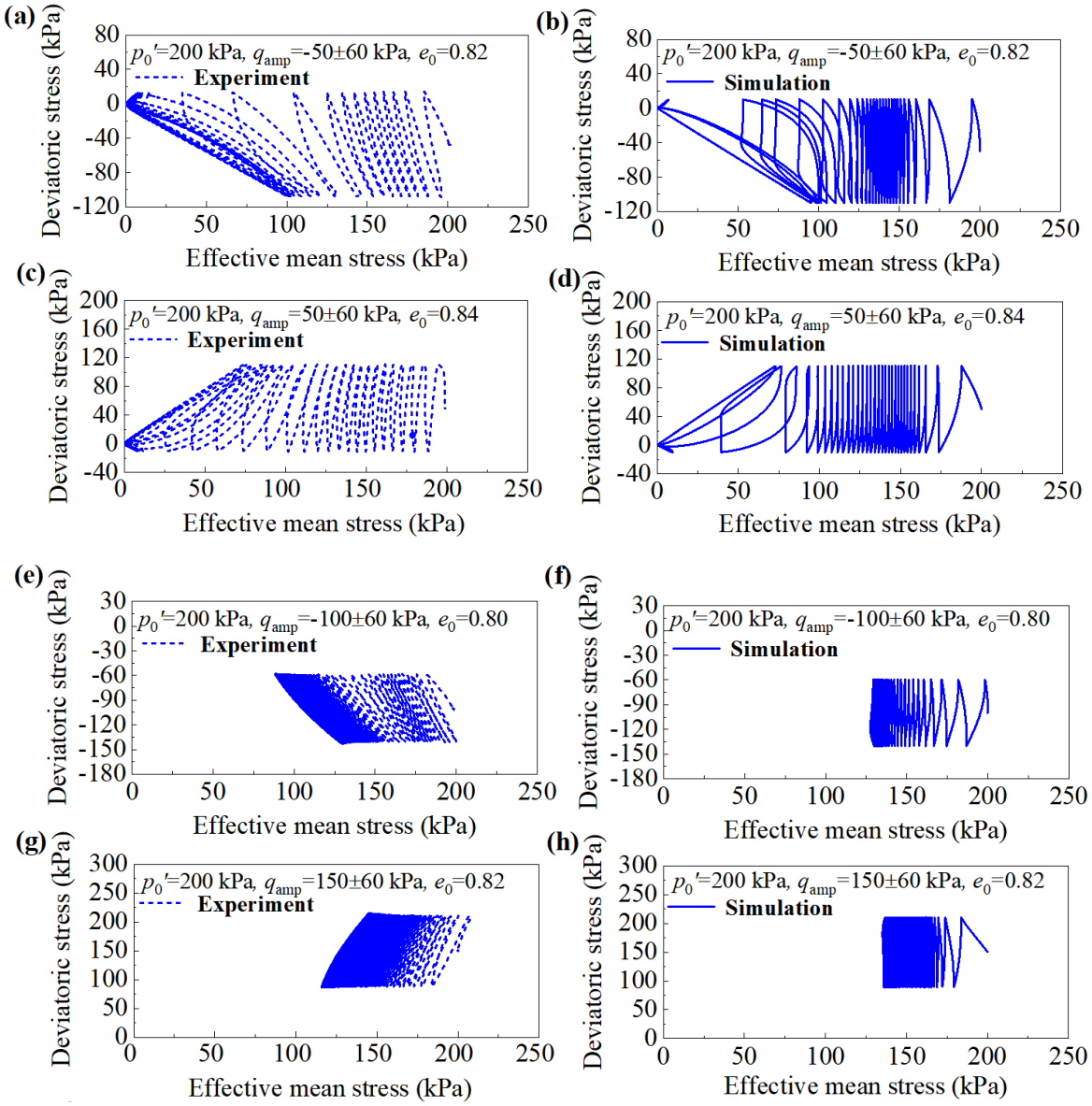

Fig. 17. Comparison between simulations and experiments of the stress path in one-way and two-way non-symmetrical undrained cyclic triaxial tests on Karlsruhe fine sand under different q_{ave} (-100, -50, 50 and 150 kPa): (a), (c), (e) and (g) experimental data from Wichtmann and Triantafyllidis (2016b); (b), (d), (f) and (h) simulations by the proposed model.

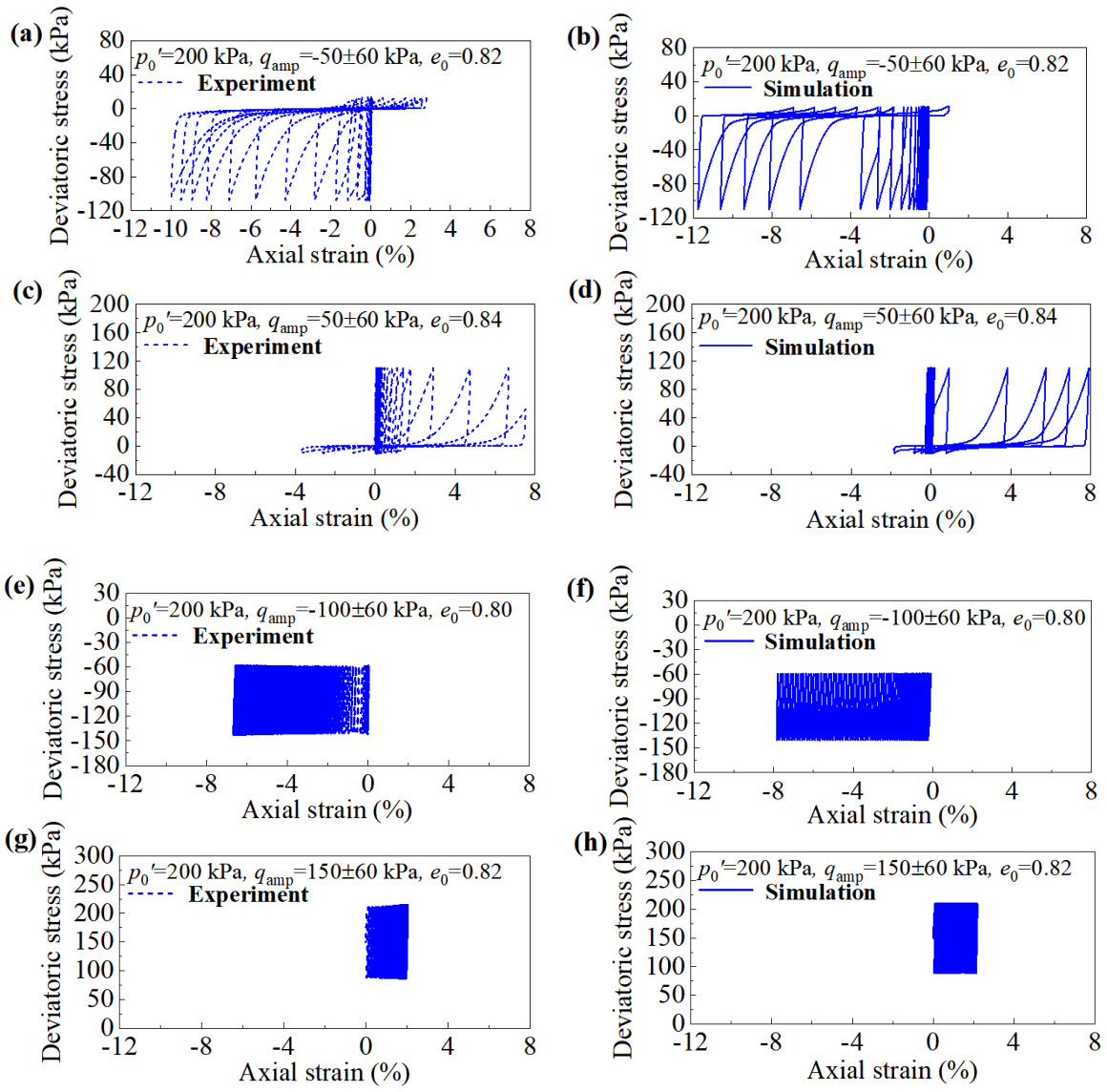

Fig. 18. Comparison between simulations and experiments of the stress-strain relations in one-way and two-way non-symmetrical undrained cyclic triaxial tests on Karlsruhe fine sand under different q_{ave} (-100, -50, 50 and 150 kPa): (a), (c), (e) and (g) experimental data from Wichtmann and Triantafyllidis (2016b); (b), (d), (f) and (h) simulations by the proposed model.

In addition to Karlsruhe fine sand, the simulation ability of the model in capturing both symmetrical and non-symmetrical two-way cyclic undrained responses of Toyoura sand is also evident, as illustrated in Figs. 21-22. The model reasonably captures the cyclic undrained responses of the sand under different cyclic amplitudes (q=-250-300kPa, ±300 kPa) in both pre-liquefaction and post-liquefaction stages, using the model constants calibrated from cyclic drained tests on Toyoura sand (Figs. 10-12).

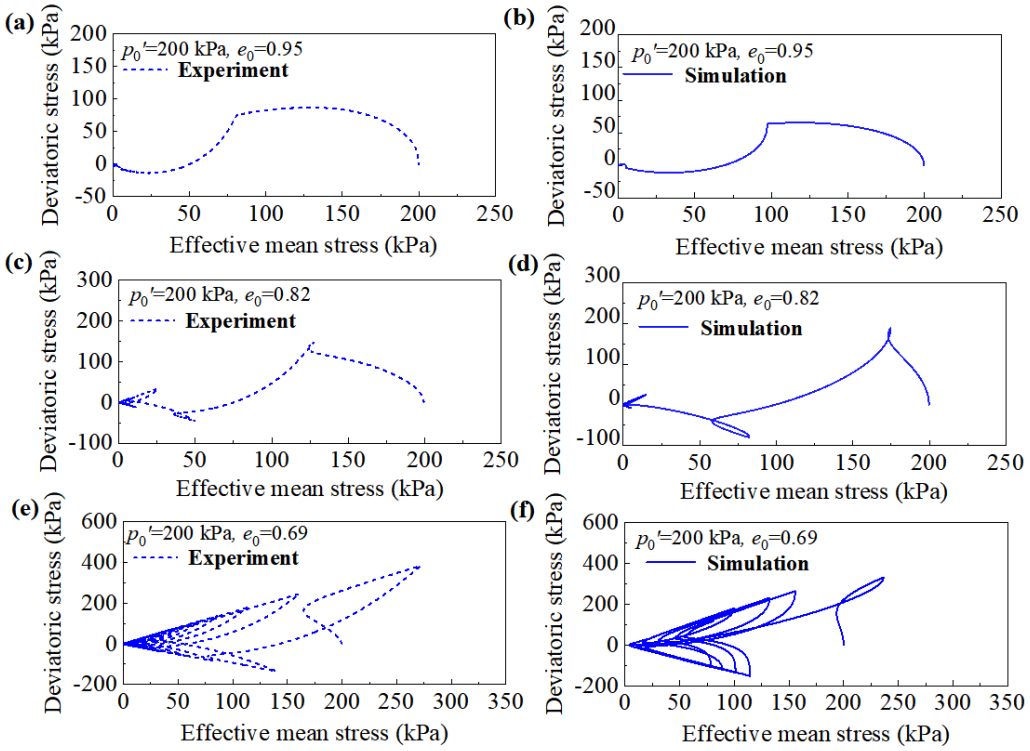

Fig. 19. Comparison between simulations and experiments of the stress path in two-way non-symmetrical undrained cyclic triaxial tests on Karlsruhe fine sand with different e_0 (i.e., 0.95, 0.82 and 0.69): (a), (c) and (e) experimental data from Wichtmann and Triantafyllidis (2016b); (b), (d) and (f) simulations by the proposed model.

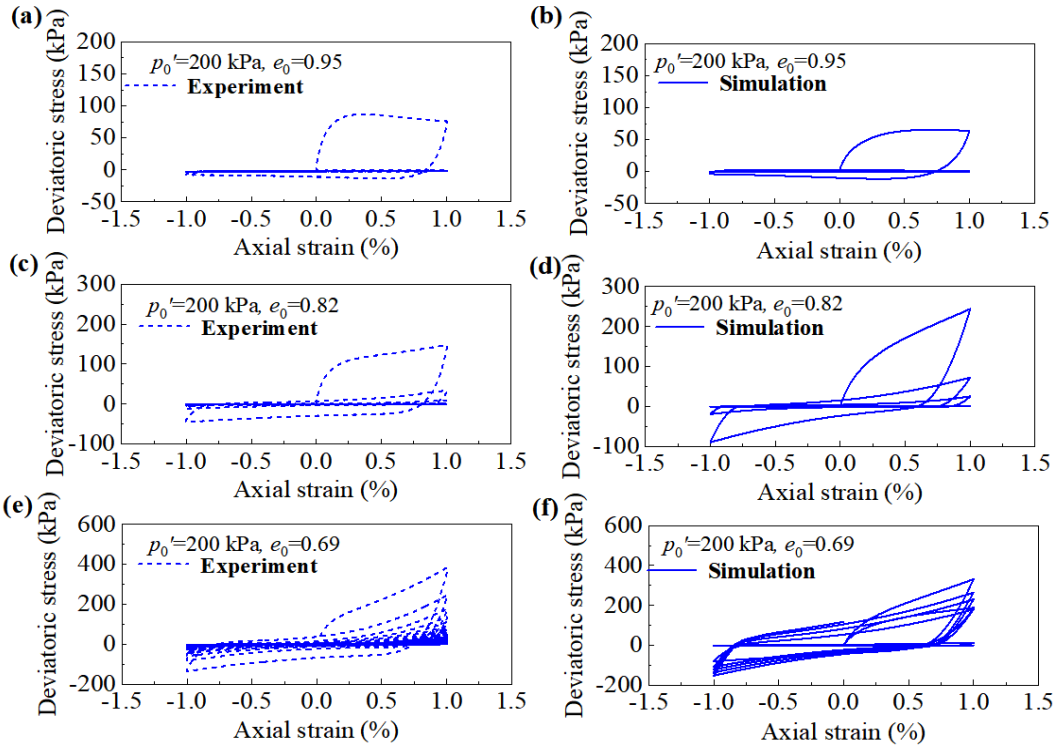

Fig. 20. Comparison between simulations and experiments of the stress-strain relations in two-way non-symmetrical undrained cyclic triaxial tests on Karlsruhe fine sand with different e_0 (i.e., 0.95, 0.82 and 0.69): (a), (c) and (e) experimental data from Wichtmann and Triantafyllidis (2016b); (b), (d) and (f) simulations by the proposed model.

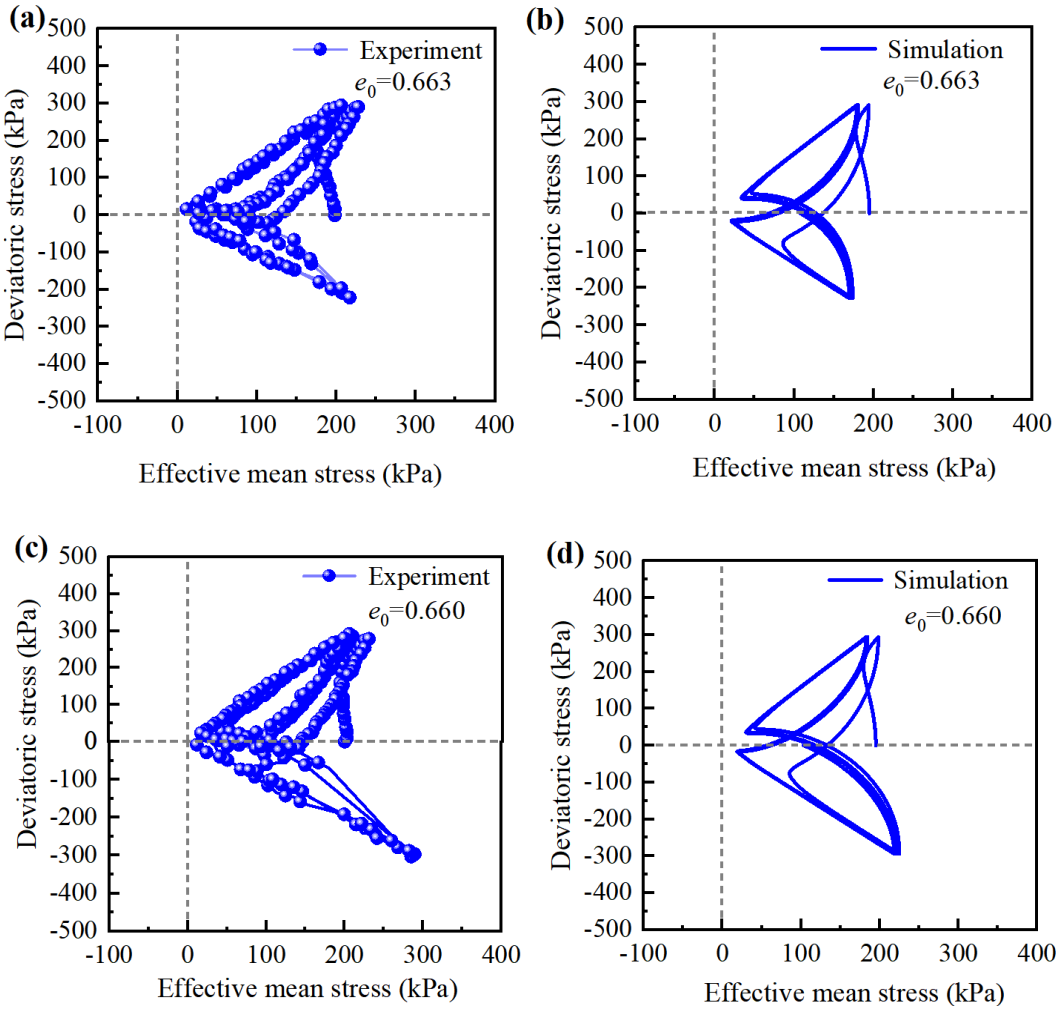

Fig. 21. Comparison between simulations and experiments of the stress path in two-way undrained cyclic non-symmetrical (q=-250 to 300 kPa) and symmetrical (q=-300 to 300 kPa) triaxial tests on Toyoura sand: (a) and (c) experimental data from Masaya et al. (2001); (b) and (d) simulations by the proposed model.

4.2.5. Undrained cyclic triaxial tests on specimens with variable bending angles

The model's ability for undrained simulation was lastly challenged to reproduce the distinct strain accumulation responses of specimens with different β_0 under a given undrained symmetrical cyclic triaxial loading. Data from three sets of such experiments performed by Oda et al. (2001) on Toyoura sand were taken for model validation. All the three specimens were prepared to have the same e_0=0.80 but with varying β_0 (i.e., 0°, 45° and 90°). Fig. 23 shows the comparisons between the measured and simulated stress-strain relationships from these tests. The model simulations match broadly with the experimental data. Particularly, the model captures the observed trends of axial strain accumulation that is non-symmetrical due to anisotropy, i.e., the axial strain predominately accumulates on the triaxial extension side for

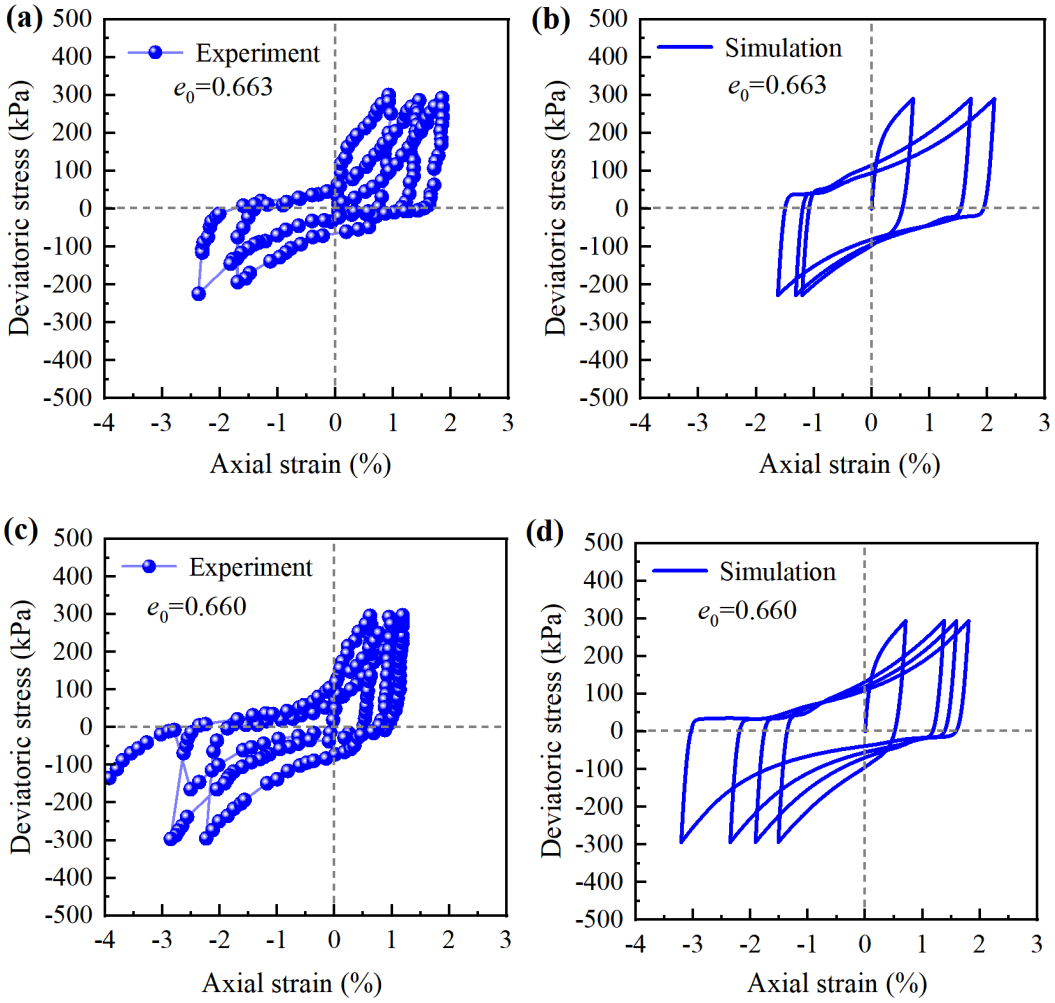

Fig. 22. Comparison between simulations and experiments of the stress-strain relations in two-way undrained cyclic non-symmetrical (q=-250 to 300 kPa) and symmetrical (q=-300 to 300 kPa) triaxial tests on Toyoura sand: (a) and (c) experimental data from Masaya et al. (2001); (b) and (d) simulations by the proposed model.

β_0=0° but on the triaxial compression side for β_0=90°. This is mainly attributed to the introduction of fabric anisotropy into dilatancy, which renders a more contractive response (higher D) for specimens with a relatively low A (e.g., β_0 =0° under TC), and thus larger cyclic strain accumulation.

5. Discussion

5.1. Role of fabric dependent dilatancy and MS hardening rules

The reasonable simulations of fabric-related responses under drained and undrained cyclic loadings, as evident in Section 4, are primarily attributed to the incorporation of fabric anisotropy A, which enters various parts of the model (as derived in Section 3). To justify the role of the exponential terms of A in dilatancy (Eq. (23)) and MS isotropic hardening (Eq.

(25)), which are the new constitutive ingredients of SANISAND-FMSf,, a comparative study is performed. The comparison is made with and without A in dilatancy and MS isotropic hardening, while the exponential functions of A are used in h and d$\mathbf{F}$ in all the comparative simulations. Two typical series of experiments on granular soils with different bedding plane angles were adopted for simulations, i.e., drained cyclic triaxial experiments performed in this study (Fig. 3a) and undrained cyclic triaxial experiments reported by Oda et al., (2001) (Fig. 23).

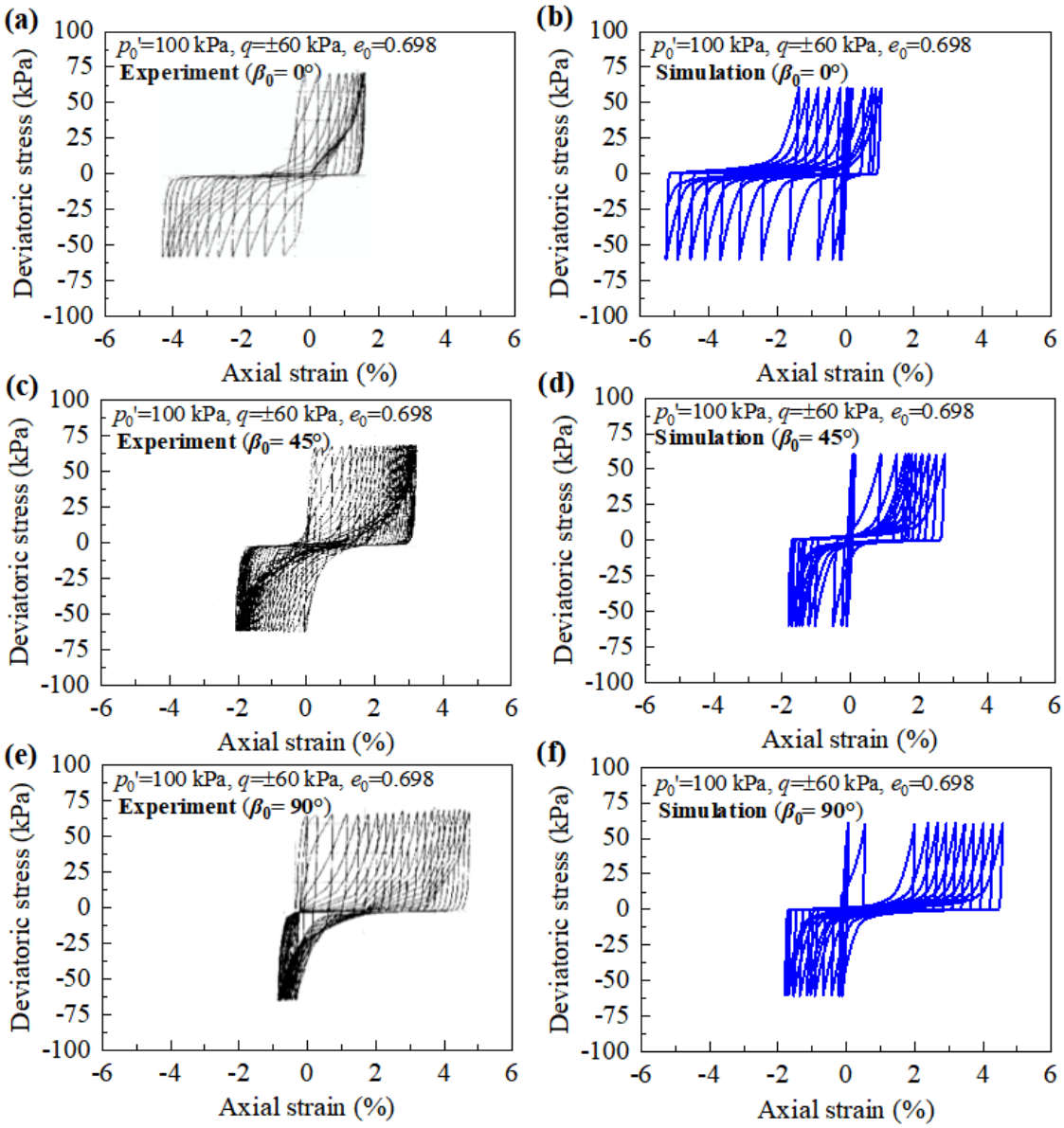

Fig. 23. Comparison between simulations and experiments of the stress-strain relations in two-way symmetrical undrained cyclic triaxial tests on Toyoura sand with different initial bedding plane angles (bedding angle β_0=0°, 45° and 90°): (a), (c) and (e) experimental data from Oda et al. (2001); (b), (d) and (f) simulations by the proposed model.

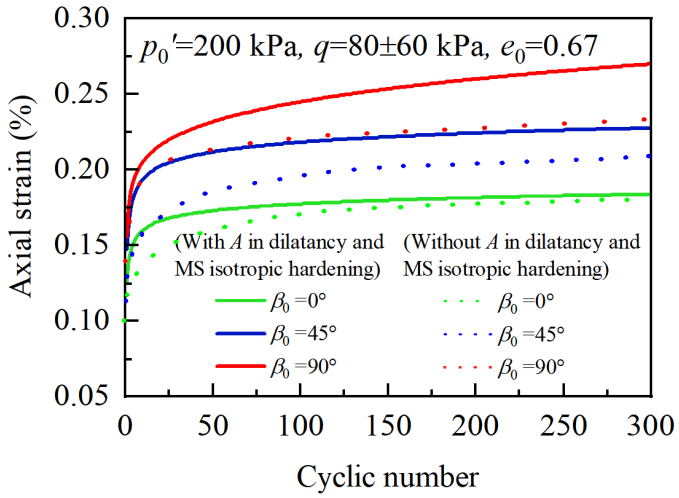

739

740 **Fig. 24.** Influence of the fabric dependent dilatancy and MS isotropic hardening with different β_0 on high-
741 cycle axial strain accumulation, with simulation settings as p_0'=200kPa, q=80±60kPa, e_0=0.67.

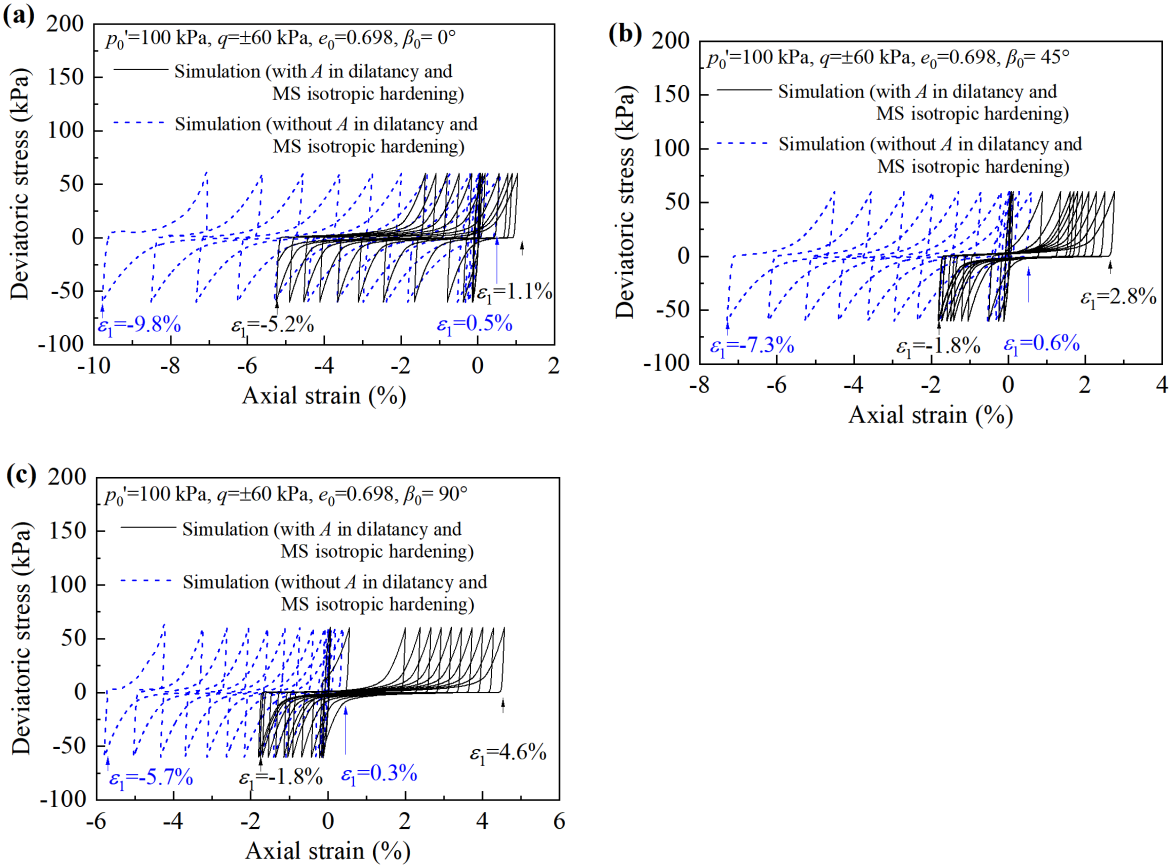

Fig. 25. Influence of the fabric dependent dilatancy and MS isotropic hardening of specimens with different β_0 under two-way undrained cyclic symmetrical loadings on simulated results: (a) β_0=0°; (b) β_0=45°; (c) β_0=90°.

742 Fig. 24 shows the influence of fabric dependent dilatancy and MS isotropic hardening on
743 simulated axial strain accumulation under drained cyclic loading, while such influence on
744 simulated stress-strain relationship under undrained cyclic loading is illustrated in Fig. 25. For

745 the cyclic drained cases (Fig. 24), the absence of fabric dependent dilatancy and MS isotropic
746 hardening in the SANISAND-FMSf model does not alter the simulated trends of strain
747 accumulation, i.e., a transition from cyclic shakedown to ratcheting by increasing initial
748 bedding plane angle β_0 from 0° to 90°. The two fabric dependent constitutive ingredients only
749 quantitatively affect the simulation results of the drained cases, with a maximum percentage
750 difference of 18% in cumulative axial strain. For the cyclic undrained cases (Fig. 25), however,
751 the absence of fabric dependent dilatancy and MS isotropic hardening in SANISAND-FMSf
752 model lead to a failure in capturing the trends of strain accumulation of specimens with different
753 β_0, i.e., much smaller straining under triaxial extension than triaxial compression for specimens
754 with β_0=45° and 90°. The additions of the two new fabric-dependent constitutive ingredients
755 enable the SANISAND-FMSf model to reasonably capture the trends and amplitudes of the
756 measured fabric-dependent undrained cyclic strain accumulation. The role of the fabric
757 dependent dilatancy and MS isotropic hardening in unified description of drained and undrained
758 cyclic strain accumulation is evident.

759 ***5.2. On the formulation of fabric evolution law***

760 The key aspect of the SANISAND-FMSf model lies in its ability to capture fabric evolution,
761 which interacts with multiple tensorial state variables and surfaces in a coupled way. A
762 simplified physical-based fabric evolution law is employed to not overcomplicate the current
763 version of the model (Papadimitriou et al., 2019). To improve the physical soundness and
764 simulation ability of the model, it is the authors' ongoing work to implement more sophisticated
765 fabric evolution laws, particularly those rigorously derived from DEM tests under complex
766 loading conditions (e.g., Sun and Sundaresan, 2011; Rojas and Kamrin, 2019). It is also worth
767 noting that for granular specimens prepared with different bedding plane angles, the fabric
768 could be some combination of contact network anisotropy and particle shape orientation.
769 Possible ways of improvements could be made by either using two orientation tensors or
770 proposing a mixed-mode fabric tensor that combines the influence of both contact anisotropy
771 and particle orientation as rendered by Wang et al. (2020). Future work will be undertaken in
772 this direction.
773

5.3. On objectivity and non-negative dissipation

Frame indifference is a fundamental rule for developing constitutive models in the framework of large deformation, where the effect of rigid-body motion should be considered in the rates of stress (Dunatunga and Kamrin, 2015) and tensorial state variables like the fabric tensor (Rojas and Kamrin, 2019). For granular soil, the strain range of engineering interests and practice is routinely within 5% (Oda et al., 2001), where the small strain assumption is still valid (Li and Dafalias, 2012). The proposed model in its present version is therefore developed in the framework of small deformation, with no inclusion of spin tensors in the evolution of stress and tensorial state variables for simplicity. An update of the present model with objective rates will be needed and can be readily achieved following Li and Dafalias (2012) for future analyses of large-deformation boundary value problems.

Non-negative dissipation (or positive entropy production) is an intended feature not always addressed in continuum plasticity modelling works, as in the model proposed here. An effort will be made to cast the model in the thermodynamics framework, by structuring free energy dependence on internal variables in conjunction with their evolution equations, to naturally satisfy the dissipation inequality with the chosen plastic flow rule. A standard approach for addressing thermodynamic compatibility in kinematic hardening models is proposed by Feigenbaum and Dafalias (2008) for metals, which could be extended to incorporate the dilatancy feature of granular soil.

6. Summary and conclusions

This study aims to understand and quantify the high-cycle deformation behavior of granular soil, through experimental investigation and constitutive modelling. Special effort is made to consider the key mechanism governing the cyclic response, i.e., the evolution of fabric anisotropy and its interplay with the loading direction, which are not explicitly addressed in the existing high-cycle experiments and models.

In the experimental study, a novel technique was adopted to prepare granular specimens with controllable fabric orientation, enabling various interplays between fabric and loading direction to be tested in a conventional cyclic triaxial apparatus. The experiments reveal that by rendering the fabric orientation closer to the loading direction (under otherwise identical

803 conditions), the high-cycle strain accumulation behavior changes remarkably, from shakedown
804 to ratcheting. Such a transition in cyclic response can be also achieved by increasing the density
805 of the granular soil or lowering the stress amplitude.

806 Inspired by experimental observations, a bounding surface plasticity model (i.e.,
807 SANISAND-MSf) accounting for the effect of fabric anisotropy and its evolution was
808 developed. The new SANISAND-FMSf model is formulated based on Yang et al. (2022)'s
809 model within classical Critical State Theory (CST), and casted it within the novel Anisotropic
810 Critical State Theory (ACST) by Li and Dafalias (2012). Following ACST, an evolving fabric
811 tensor **F** is introduced, and its interplay with the loading direction **n** is characterized by defining
812 a fabric anisotropy variable A=**F**:**n**. A is then incorporated into the dilatancy state parameter ζ,
813 which enters the formulations for the dilatancy and plastic modulus via the dependence of
814 dilatancy surface and bounding surface on it. Two novel constitutive ingredients are proposed,
815 i.e., new dilatancy function and MS isotropic hardening rule (which naturally links to the
816 kinematic hardening rule) considering effects of evolving fabric anisotropy. Dependency of the
817 hardening modulus parameter h and the evolution equation of the fabric tensor **F** on A have
818 been proposed earlier by Papadimitriou et al (2019) and Petalas et al (2020), and were adopted
819 in the SANISAND-FMSf model.

820 The simulation capability of the model is validated against a dataset of three sands (Fujian
821 sand, Karlsruhe fine sand and Toyoura sand) which cover a wide range of initial states, various
822 anisotropy (including fabric and stress anisotropy), multiple cyclic loading types under both
823 drained and undrained conditions. The model can unify the description of high-cycle strain
824 accumulation (i.e., shakedown and ratcheting) under drained conditions, as well as pre-
825 liquefaction and post-liquefaction cyclic responses of each given sand using a unified set of
826 constants. The new SANISAND-FMSf model exhibits a unique feature of simulating the
827 distinct high-cycle strain accumulation and liquefaction of granular material with various fabric
828 anisotropy, while the existing high-cycle models treat them equally. It confirms the correctness
829 and usefulness of Li and Dafalias (2012)'s general theoretical framework in transforming any
830 given constitutive model constructed from the classical CST to ACST.

831 The new SANISAND-FMSf model can be readily implemented into finite element codes.
832 This would be useful to future applications in offshore, transportation and earthquake

833 engineering, where quantitative whole-life assessment of various foundations on anisotropic
834 granular soils under high-cycle loading events remains to be a challenging but critical issue.

835 **Acknowledgements**

836 The authors gratefully acknowledge the financial supports provided by National Natural
837 Science Foundation of China (52122906, 52238001 and 51939010), Finance Science and
838 Technology Project of Hainan Province (ZDKJ202019), and the Zhejiang Provincial Natural
839 Science Foundation (Grant No. LHZ20E090001) and the Royal Society International
840 Exchanges Grant (Grant No. IEC\NSFC\223020). The authors are also grateful to Mr Li Wenke
841 for performing some high-cycle experiments, and Mr Chen Qijian for calibrating model
842 constants.
843

References

Barrero, A. R., Taiebat, M., Dafalias, Y.F., 2020. Modeling cyclic shearing of sands in semifluidized regime. Int. J. Numer. Anal. Methods Geomech. 44(3), 371-388.

Bian, X., Jiang, H., Chang, C., Hu, J., Chen, Y., 2015. Track and ground vibrations generated by high-speed train running on ballastless railway with excitation of vertical track irregularities. Soil Dyn. Earthq. Eng. 76, 29-43.

Been, K., Jefferies M.G., 1985. A state parameter for sands. Géotechnique. 35(2),99-112.

Borja, R.I., Song, X., Rechenmacher, A.L., Abedi, S., Wu, W., 2013. Shear band in sand with spatially varying density. J. Mech. Phys. Solids. 61(1), 219-234.

Chiaro G., Koseki J., Sato T., 2012. Effects of initial static shear on liquefaction and large deformation properties of loose saturated Toyoura sand in undrained cyclic torsional shear tests. Soils Found. 52(3), 498-510.

Chiu, C.F., Ng, C.W.W., 2003. A state-dependent elasto-plastic mode for saturated and unsaturated soils. Géotechnique. 53(9), 809-829.

Corti, R., Diambra, A., Wood, D.M., Escribano, D.E., Nash, D.F.T., 2016. Memory surface hardening model for granular soils under repeated loading conditions. J. Eng. Mech. 142 (12), 04016102.

Dafalias, Y.F., Popov, E.P., 1975. A model of nonlinearly hardening materials for complex loading. Acta Mech. 21(3), 173-192.

Dafalias, Y.F., Popov, E.P., 1976. Plastic internal variables formalism of cyclic plasticity. J. Appl. Mech. 43(4), 645-651.

Dafalias, Y.F., 1986. Bounding surface plasticity. I: mathematical foundation and hypoplasticity. J. Eng. Mech. 112(9), 966-987.

Dafalias, Y.F., Herrmann, L.R., 1986. Bounding surface plasticity. II: Application to isotropic cohesive soils. J. Eng. Mech. 112(12), 1263-1291.

Dafalias, Y.F., Manzari, M.T., 2004. Simple plasticity sand model accounting for fabric change effects. J. Eng. Mech. 130(6), 622-634.

Dafalias, Y.F., Papadimitriou, A.G., Li, X.S., 2004. Sand Plasticity Model Accounting for Inherent Fabric Anisotropy. J. Eng. Mech. 130(11), 1319-1333.

Deng, N., Wautier, A., Thiery, Y., Yin, Z.Y., Hicher, P.Y., Nicot, F., 2021. On the attraction power of critical state in granular materials. J. Mech. Phys. Solids. 149, 104300.

Dunatunga, S., Kamrin, K., 2015. Continuum modelling and simulation of granular flows through their many phases. J. Fluid. Mech. 779.

Feigenbaum, H.P., Dafalias, Y.F., 2008. Simple model for directional distortional hardening in metal plasticity within thermodynamics. J. Eng. Mech. 134(9), 730-738.

Gao, Z.W., Zhao, J.D., Li, X.S., Dafalias, Y.F., 2014. A critical state sand plasticity model accounting for fabric evolution. Int. J. Numer. Analyt. Meth. Geomech. 38(4), 370-390.

Gao, Z.W., Zhao, J.D., 2015. Constitutive Modeling of Anisotropic Sand Behavior in Monotonic and Cyclic Loading. J. Eng. Mech. 141(8):04015017.

Gajo, A., Muir Wood, D., 1999. Severn-Trent sand: a kinematic hardening constitutive model for sands: the *q-p* formulation. Géotechnique. 49(5), 595-614.

Hong, Y., Wang, X.T., Wang, L.Z., Gao, Z.W., 2021. A state-dependent constitutive model for coarse-grained gassy soil and its application in slope instability modelling. Comput. Geotech. 129, 103847.

Houlsby, G.T., Abadie, C.N., Beuckelaers, W.J.A.P., Byrne, B.W., 2017. A model for nonlinear hysteretic and

887 ratcheting behaviour. Int. J. Solids. Struct. 120, 67-80.
888 Huang, E., Marks, B., Einav, I., 2020. Continuum homogenisation of stochastic comminution with grainsize
889 fabric. J. Mech. Phys. Solids. 103897.
890 Indraratna, B., Nimbalkar, S., 2013. Stress-strain degradation response of railway ballast stabilized with
891 geosynthetics. J. Geotech. Geoenviron. Eng. 139(5), 684-700.
892 Iwashita, K., Oda, M., 1999. Micro-deformation mechanism of shear banding process based on modified
893 distinct element method. Powder. Technol. 109(1), 192-205.
894 Jardine, R. J., 2020. Geotechnics, energy and climate change: the 56th Rankine Lecture. Géotechnique, 70(1),
895 3-59.
896 Karapiperis, K., Harmon, J., Andò, E., Viggiani, G., Andrade, J.E., 2020. Investigating the incremental
897 behavior of granular materials with the Level-Set Discrete Element Method. J. Mech. Phys. Solids. 144,
898 104103.
899 Kang, G., 2008. Ratchetting: Recent progresses in phenomenon observation, constitutive modeling and
900 application. Int. J. Fatigue. 30(8),1448-1472.
901 Krieg, R. D., 1975. A practical two surface plasticity theory. J. Appl. Mech. 42(3): 641-646.
902 LeBlanc, C., Houlsby, G.T., Byrne, B.W., 2010. Response of stiff piles in sand to long-term cyclic lateral
903 loading. Géotechnique. 60(2), 79-90.
904 Li, X.S., Dafalias, Y.F., 2000. Dilatancy for cohesionless soils. Géotechnique. 50(4): 449-460.
905 Li, X.S., Li, X., 2009. Micro-macro quantification of the internal structure of granular materials. J. Eng.
906 Mech. 135:7(641), 641-656.
907 Li, X.S., Dafalias, Y.F., 2012. Anisotropic critical state theory: Role of fabric. J. Eng. Mech. 0000324, 263-
908 275.
909 Li, X.S., Dafalias, Y.F., 2015. Dissipation consistent fabric tensor definition from DEM to continuum for
910 granular media. J. Mech. Phys. Solids. 78, 141-153.
911 Liao, D., Yang, Z.X., 2021. Hypoplastic modeling of anisotropic sand behavior accounting for fabric
912 evolution under monotonic and cyclic loading. Acta Geotech. 16, 2003-2029.
913 Liu, H.Y., Abell, J.A., Diambra, A., Pisano, F., 2019. Modelling the cyclic ratcheting of sands through
914 memory-enhanced bounding surface plasticity. Géotechnique. 69(9), 783-800.
915 Manzari, M.T., Dafalias, Y.F., 1997. A two-surface critical plasticity model for sand. Géotechnique. 47(2),
916 255-272.
917 Masaya, H., Nakai, T., Hoshikawa, T., Yoshida, H. 2001. Dilatancy characteristic and anisotropy of sand
918 under monotonic and cyclic loading. Soils. Found. 41(3), 107-124.
919 Miura, S., Toki, S., 1984. Anisotropy in mechanical properties and its simulation of sands sampled from
920 natural deposits. Soils. Found. 24(3): 69-84.
921 Nemat-Nasser, S., 2000., A micromechanically-based constitutive model for frictional deformation of
922 granular materials. J. Mech. Phys. Solids. 48(6), 1541-1563.
923 Niemunis, A., Herle, I., 1997. Hypoplastic model for cohesionless soils with elastic strain range. Mech.
924 Cohes.-frict. Mater. 2(4), 279-299.
925 Oda, M., Kawamoto, K., Suzuki, K., Fujimori, H., Sato, M., 2001. Microstructural interpretation on
926 reliquefaction of saturated granular soils under cyclic loading. J. Geotech. Geoenviron. Eng. 127(5),
927 416-423.
928 Papadimitriou, A.G., Chaloulos, Y.K., Dafalias, Y.F., 2019. A fabric-based sand plasticity model with reversal
929 surfaces within anisotropic critical state theory. Acta Geotech.14(2), 253-277.
930 Page, A.M., Klinkvort, R.T., Bayton, S., Zhang, Y., Jostad, H.P., 2021. A procedure for predicting the

permanent rotation of monopiles in sand supporting offshore wind turbines. Mar. Struct. 75: 102813.
Petalas A.L., Dafalias, Y.F., Papadimitriou A.G., 2019. SANISAND-FN: An evolving fabric-based sand model accounting for stress principal axes rotation. Int. J. Num. Anal. Meth. Geomechanics. 43(1), 97-123.
Petalas, A.L., Dafalias, Y.F., Papadimitriou, A.G., 2020. SANISAND-F: Sand Constitutive Model with Evolving Fabric Anisotropy. Int. J. Solids. Struct. 43(12), 2041-2055.
Richard, F.E., Hall, J.R., Woods, R.D., 1970. Vibrations of soils and foundations. Prentice Hall Inc., Englewood Cliffs, New Jersey.
Rojas, P.E., Kamrin, K., 2019. Capturing transient granular rheology with extended fabric tensor relations. Granul. Matter. 21, 1-7.
Sibille, L., Hadda, N., Nicot, F., Tordesillas, A., Darve, F., 2015. Granular plasticity, a contribution from discrete mechanics. J. Mech. Phys. Solids. 75, 119-139.
Song, D., Yu, C., Zhang, C., Kang, G., 2023. Superelasticity degradation of NiTi shape memory alloy in wide ranges of temperature and loading level: Experimental observation and micromechanical constitutive model. Int. J Plasticity, 161, 103487.
Sun, J., Sundaresan, S., 2011. A constitutive model with microstructure evolution for flow of rate-independent granular materials. J. Fluid. Mech. 682, 590-616.
Taiebat, M., Dafalias, Y. F., 2008. SANISAND: simple anisotropic sand plasticity model. Int. J. Numer. Analyt. Methods Geomech. 32(8) , 915-948.
Theocharis A.I., Vairaktaris, E., Dafalias, Y.F., Papadimitriou, A.G., 2017. Proof of incompleteness of Critical State Theory in granular mechanics and its remedy, J. Eng. Mech. 143(2), 04016117.
Theocharis, A.I., Vairaktaris, E., Dafalias, Y.F., Papadimitriou, A.G. 2019. Necessary and sufficient conditions for reaching and maintaining critical state. Int. J. Num. Anal. Meth. Geomechanics. 43(12), 2041-2055.
Wang, L.Z., Wang, H., Zhu, B., Hong, Y., 2018. Comparison of monotonic and cyclic lateral response between monopod and tripod bucket foundations in medium dense sand. Ocean Eng. 155, 88-105.
Wang, R., Cao, W., Xue, L., Zhang J.M., 2021. An anisotropic plasticity model incorporating fabric evolution for monotonic and cyclic behavior of sand. Acta Geotech. 16(1), 43-65.
Wichtmann, T., 2005. Explicit accumulation model for non-cohesive soils under cyclic loading. PhD thesis, Institut für Grundbau und Bodenmechanik, Bochum University, Bochum, Germany.
Wichtmann, T., Triantafyllidis, T., 2016a. An experimental database for the development, calibration and verification of constitutive models for sand with focus to cyclic loading: Part II-Tests with strain cycles and combined loading. Acta Geotech. 11(4), 763-774.
Wichtmann, T., Triantafyllidis, T., 2016b. An experimental database for the development, calibration and verification of constitutive models for sand with focus to cyclic loading: part I-tests with monotonic loading and stress cycles. Acta Geotech. 11(4), 739-761.
Wu, W., Bauer, E., Kolymbas, D., 1996. Hypoplastic constitutive model with critical state for granular materials. Mech. Mater. 23(1): 143-163.
Yang, M., Taiebat, M., Dafalias, Y.F., 2022. SANISAND-MSf: a sand plasticity model with memory surface and semifluidised state. Géotechnique. 72(3), 227-246.
Yang, J., Luo, X.D., 2015. Exploring the relationship between critical state and particle shape for granular materials. J. Mech. Phys. Solids. 84, 196-213.
Yu, C., Kang, G., Kan, Q., 2015. A micromechanical constitutive model for anisotropic cyclic deformation of super-elastic NiTi shape memory alloy single crystals. J. Mech. Phys. Solids. 82, 97-136.

975 Yang, Z.X., Xu, T.T., Chen, Y.N., 2018. Unified modeling of the influence of consolidation conditions on
976 monotonic soil response considering fabric evolution. J. Eng. Mech. 144(8), 04018073.
977 Yin, Z.Y., Chang, C.S., Hicher, P.Y., 2010. Micromechanical modelling for effect of inherent anisotropy on
978 cyclic behaviour of sand. Int. J. Solids. Struct. 47(14-15), 1933-1951.
979